Gondwana Research 82 (2020) 48–72

Contents lists available at ScienceDirect

Gondwana Research

journal homepage: www.elsevier.com/locate/gr

Petrogenesis of the ~740 Korab Kansi mafic-ultramafic intrusion, South Eastern Desert of Egypt: Evidence of Ti-rich ferropicritic magmatism

Mohamed Zaki Khedr [a,*], Amr El-Awady [b], Shoji Arai [c], Christoph Hauzenberger [d], Akihiro Tamura [c], Robert J. Stern [e], Tomoaki Morishita [c]

[a] Department of Geology, Faculty of Science, Kafrelsheikh University, 33516 Kafrelsheikh, Egypt
[b] Geology Department, Faculty of Science, Zagazig University, Zagazig 44519, Egypt
[c] Department of Earth Sciences, Kanazawa University, Ishikawa 920-1192, Japan
[d] Institute of Earth Sciences - NAWI Graz Geocenter, Karl-Franzens-Universität Graz, 28010 Graz, Austria
[e] Geosciences Department, University of Texas at Dallas, Richardson, TX 75083-0688, USA

ARTICLE INFO

Article history:
Received 11 September 2019
Received in revised form 18 December 2019
Accepted 20 December 2019
Available online 30 January 2020

Keywords:
layered intrusion
gabbroic rocks
ferropicritic melt
Fe-Ti oxides
island arc setting, Egypt

ABSTRACT

The Neoproterozoic Korab Kansi mafic-ultramafic intrusion is one of the largest (100 km^2) intrusions in the Southern Eastern Desert of Egypt. The intrusion consists of Fe-Ti-bearing dunite layers, amphibole peridotites, pyroxenites, troctolites, olivine gabbros, gabbronorites, pyroxene gabbros and pyroxene-hornblende gabbros, and also hosts significant Fe-Ti deposits, mainly as titanomagnetite-ilmenite. These lithologies show rhythmic layers and intrusive contacts against the surrounding granites and ophiolitic-island arc assemblages. The wide ranges of olivine forsterite contents ($Fo_{67.9-85.7}$), clinopyroxene Mg# (0.57–0.95), amphibole Mg# (0.47–0.88), and plagioclase compositions ($An_{85.8-40.9}$) indicate the role of fractional crystallization in the evolution from ultramafic to mafic rock types. Clinopyroxene (Cpx) has high REE contents (2–30 times chondrite) with depleted LREE relative to HREE, like those crystallized from ferropicritic melts generated in an island-arc setting. Melts in equilibrium with Cpx also resemble ferropicrites crystallized from olivine-rich mantle melts. Cpx chemistry and its host rock compositions have affinities to tholeiitic and calc-alkaline magma types. Compositions of mafic-ultramafic rocks are depleted in HFSE (e.g. Nb, Ta, Zr, Th and U) relative to LILE (e.g. Li, Rb, Ba, Pb and Sr) due to the addition of subduction-related hydrous fluids (rich in LILE) to the mantle source, suggesting an island-arc setting. Fine-grained olivine gabbros may represent quenched melts approximating the primary magma compositions because they are typically similar in assemblage and chemistry as well as in whole-rock chemistry to ferropicrites. We suggest that the Korab Kansi intrusion crystallized at temperatures ranging from ~700 to 1100 °C from ferropicritic magma derived from melting of metasomatized mantle at <5 Kbar. These hydrous ferropicritic melts were generated in the deep mantle and evolved by fractional crystallization under high fO_2 at relatively shallow depth. Fractionation formed calc-alkaline magmas during the maturation of an island arc system, reflecting the role of subduction-related fluids. The interaction of metasomatized lithosphere with upwelling asthenospheric melts produced the Fe and Ti-rich ferropicritic parental melts that are responsible for precipitating large quantities of Fe-Ti oxide layers in the Korab Kansi mafic-ultramafic intrusion. The other factors controlling these economic Fe-Ti deposits beside parental melts are high oxygen fugacity, water content and increasing degrees of mantle partial melting. The generation of Ti-rich melts and formation of Fe-Ti deposits in few layered intrusions in Egypt possibly reflect the Neoproterozoic mantle heterogeneity in the Nubian Shield. We suggest that Cryogenian-Tonian mafic intrusions in SE Egypt can be subdivided into Alaskan-type intrusions that are enriched in PGEs whereas Korab Kansi-type layered intrusions are enriched in Fe-Ti-V deposits.

1. Introduction

Mafic-ultramafic intrusions are widespread in the northern part of the Nubian Shield, outcropping mainly in the Southern Eastern Desert (SED) of Egypt. SED mafic-ultramafic intrusions are classified into three groups that are distinguished according to their emplacement in different tectonic settings: 1) ophiolitic rocks (mainly 770 to ~720 Ma; Ali et al., 2009) that represent remnant sections of forearc mantle and crust that occur mostly along major shear zones (e.g., Arais-Abu Dahr; Khedr and Arai, 2013, 2016a), 2) Alaskan-type ultramafic–mafic rocks (711 ± 7 Ma U-Pb zircon age, Dixon, 1981; Sm/Nd model age of 770 ± 20 Ma for Abu Hamamid, Farahat and Helmy, 2006; Sm-Nd age of 963 ± 81 Ma for Genina Gharbia,

* Corresponding author.
E-mail address: mohamed.khader1@sci.kfs.edu.eg (M.Z. Khedr).

https://doi.org/10.1016/j.gr.2019.12.013
1342-937X/

Helmy et al., 2014) occurring as concentrically zoned intrusions and representing roots of Neoproterozoic island arcs (e.g. Gabbro Akarem, Helmy and El Mahallawi, 2003; Genina Gharbia, Helmy et al., 2014; Abu Hamamid, Helmy et al., 2015; Dahanib, Khedr and Arai, 2016b), and 3) post orogenic layered mafic-ultramafic intrusions related to late extension (e.g., Imleih; Azer and El-Gharbawy, 2011; Motaghairat; Abdel Halim et al., 2016) and intruded late in the evolution of this crust (<640 Ma; Be'eri-Shlevin et al., 2009). Each provides important information on the chemical history of the mafic-ultramafic parental mantle source and its tectonic setting. The origin and tectonic settings of mafic-ultramafic intrusions in Egypt are still a matter of debate. However, it is generally accepted that volatile-bearing mantle plumes or mantle upwelling of asthenosphric melts may play an important role in origin and formation of mafic-ultramafic intrusions (Pirajno, 2004; Mao et al., 2008; Fiorentini et al., 2008; Khedr and Arai, 2016b).

The mafic-ultramafic intrusions in Egypt are economically significant, where types of ore deposits may depend on the origin or type of these intrusions and can be used to classify these intrusions. For instance, ED Alaskan-type mafic-ultramafic intrusions such as Gabbro Akarem (Helmy and Mogessie, 2001) and Genina Gharbia (Helmy, 2004) may host sub-economic Cu–Ni-S-PGE deposits, but several Fe-Ti-rich mafic-ultramafic layered intrusions host economic ilmenite-titanomagnetite deposits such as Abu Ghalaga, Korab Kansi, Gabal Akab El Negum and Wadi Abu Fas. The ED Abu Ghalaga mine has the largest Fe-Ti ore reserve (Nasr et al., 2000; Makhlouf et al., 2008). The Korab Kansi layered mafic-ultramafic complex is one of the largest (about 100 km^2) layered intrusions in the SED of Egypt. It hosts significant Fe-Ti oxide deposits, and ranks second in ore reserves after Abu Ghalaga. It is rich in Fe-Ti deposits, like some Egyptian layered intrusions, but also poor in Cu–Ni-S-PGE deposits of Alaskan-type origin. The Fe-Ti oxide deposits in the Korab Kansi intrusion are found as disseminated oxides or as layers of massive titanomagnetite-ilmenite. The generation of Ti-rich parental melts and formation of Fe-Ti deposits in a few layered intrusions possibly reflect involvement of anomalously Fe-Ti enriched mantle by upwelling asthenospheric melts and/or recycled oceanic crust (Jennings et al., 2016), reflecting Neoproterozoic mantle heterogeneity. The generation of parent ferropicritic melts of the Korab Kansi intrusion in the Nubian Shield is the evidence for lithological heterogeneity in their mantle source (Fiorentini et al., 2008).

The Korab Kansi mafic-ultramafic intrusion provides important information about how the Nubian-Shield crust formed, and how this Shield evolved during the reconstruction of Gondwanaland. It also represents a natural laboratory for studying both magmatic (e.g., differentiation, assimilation, mixing) and cumulate processes within the mantle and crust. The origin of the Korab Kansi mafic-ultramafic intrusion is still debated. It has been described as an intrusive metagabbro-diorite complex that formed in an island arc setting (El-Ramly, 1972), as a layered ophiolitic metagabbro (Kröner et al., 1992; Zimmer et al., 1995) and as a layered mafic-ultramafic intrusion (Abdel-Gawad, 2002; Makhlouf et al., 2008). The Korab Kansi intrusion is associated with island-arc assemblages, shows layers, and its mineral chemistry, whole rock chemistry and ore deposits suggest the layered origin not the Alaskan origin. The present study is the first to present detailed mineralogy, petrology and geochemistry of the Korab Kansi intrusion and use these data to address the origin and significance of these rocks that host economic titanomagnetite-ilmenite deposits. The factors controlling these economic Fe-Ti deposits are also discussed in this work. The aim of this study is to shed light on petrogenesis and geodynamic evolution of the Korab Kansi intrusion as well as to understand the significance of Neoproterozoic Ti-rich ferropicritic magmatism in the Nubian Shield. This study can also elucidate the Neoproterozoic evolution of this part of Gondwanaland throughout understanding magmatic types and evolution of the Nubian Shield.

2. Geologic setting of Korab Kansi intrusion

The Korab Kansi intrusion is located in the SED of Egypt (Fig. 1a) to the west of Gabal El Gerf in the geologic map of Marsa Sha'ab quadrangle (GSE, 2002), and covers an area of about 100 km^2 (Fig. 1b). It lies along the E-W Allaqi-Heiani suture, where the N-S Hamisana shear zone (HSZ) cuts it (Stern et al., 1989). The HSZ separates the Korab Kansi intrusion from ophiolitic mafic-ultramafic bodies to the east including El-Gerf and Abu Hudeid (Stern et al., 1989; GSE, 2002). The HSZ was the site of intensive thermal and tectonic activity at 550–660 Ma, postdating the Korab Kansi intrusion (Stern et al., 1989).

The age and radiogenic isotopic composition of the Korab-Khansi intrusion was determined by Kröner et al. (1992) and Zimmer et al. (1995), although they mistakenly thought it was part of the Gerf ophiolite. Kröner et al. (1992) determined a zircon evaporation Pb-Pb age for layered gabbro (sample GG260) of 741 ± 21 Ma, while granites that crosscut layered gabbro have zircon ages of 713 ± 12 Ma. These layered gabbros also gave an age of 720 ± 9 Ma based on a 16-point Sm-Nd whole-rock isochron (Zimmer, 1989; Zimmer et al., 1995). Zimmer et al. (1995) also determined $^{87}Sr/^{86}Sr = 0.7024$ to 0.7029 and ε-Nd(t) = +4.5 to +7.9 for these rocks. The Korab Kansi intrusion is younger than the El Gerf ophiolite group and older than surrounding syntectonic granites (Fig. 1). It is a syntectonic intrusion because it was intruded by syntectonic granites (Fig. 1c, Fig. 2e).

Compression associated with the HSZ affected the Korab Kansi intrusion, causing the formation of an open fold with Fe-Ti oxide-rich dunite layers exposed near the fold axis (Makhlouf et al., 2008). These oxide-rich dunite layers also show compression-related pinch and swell structure (Fig. 2a). Several sets of faults trending E-W, ENE-WSW and NW-SE are observed (Abdel-Gawad, 2002; Makhlouf et al., 2008) (Fig. 1b, Supplementary 1). E-W trending faults along Wadi Kamwib (Fig. 1b) are right-lateral strike-slip faults that affect Fe-Ti oxide-rich dunite layers, causing discontinuities (Fig. 2b). E-W faults are also found along Wadi Wadhait (Fig. 1b). ENE-WSW-trending right-lateral strike-slip faults affect the northern part of the intrusion (Abdel-Gawad, 2002; Makhlouf et al., 2008). A NNW-SSE trending normal fault along Wadi Seyet parallels the HSZ (El-Kazzaz, 2012). NW-SE normal faults with variable dips also disrupt the Fe-Ti oxide-rich dunite layers, forming a horst structure (Makhlouf et al., 2008).

Based on the geologic map of the Marsa Sha'ab quadrangle (GSE, 2002), the Korab Kansi area consists mainly of a Neoproterozoic mafic-ultramafic intrusion (mainly gabbroic rocks) in the south and ophiolitic mélange such as serpentinites and talc carbonate nappes in the north; these mélange rocks are intruded by the Korab Kansi mafic-ultramafic body along their southern to southeastern margin (Fig. 1b). Gabbroic rocks are mainly pyroxene gabbros and pyroxene-hornblende gabbros (>75 vol%) with subordinate olivine gabbros, troctolites, and gabbronorites (Fig. 1b; Supplementary 1). Gabbros sometimes contain xenoliths and enclaves of serpentinites and talc-carbonates within their margin near the contact with serpentinites (Fig. 2f). They show thermal effects against the ultramafic rocks they contact. On its eastern margin, the Korab Kansi body also intrudes felsic to intermediate volcanic schists, calc-alkaline metavolcanics and volcanogenic metasediments (island-arc association) (Fig. 1b, Supplementary 1). The Korab Kansi intrusion is intruded from the south and west by syn-tectonic biotite ± hornblende tonalites, granodiorites and quartz diorites (syn-tectonic granites; Fig. 1b, c), showing sharp intrusive contacts (Fig. 2e, Abdel-Gawad, 2002). Apophyses of syn-tectonic granitoids extend into the gabbros (Fig. 2e). Granitoids also include xenoliths of the mafic-ultramafic rocks, mainly pyroxene gabbro (Abdel-Gawad, 2002), indicating that the syntectonic granites are younger and intrude it. The Korab Kansi mafic-ultramafic intrusion intrudes into both island-arc association in the east and ophiolitic serpentinites in the northern part of the studied area, forming a sharp intrusive contact (Fig. 2d), without any evidence of tectonic or thrust contacts (Fig. 1). Chilled margins were observed in the north and northwestern

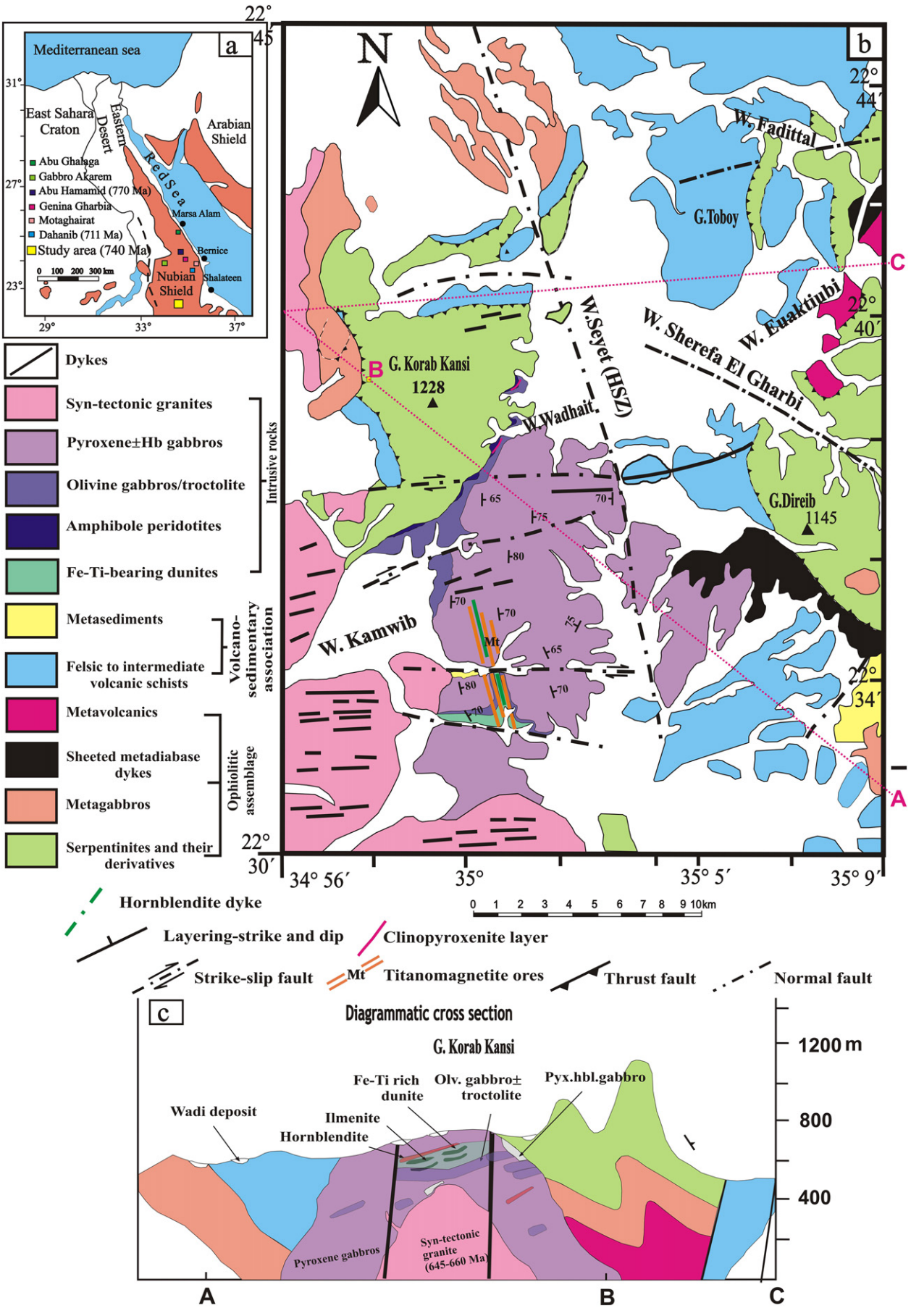
a
Mediterranean sea
East Sahara Craton
Eastern Desert
Red Sea
Arabian Shield
Nubian Shield
Marsa Alam
Bernice
Shalateen
Abu Ghalaga
Gabbro Akarem
Abu Hamamid (770 Ma)
Genina Gharbia
Motaghairat
Dahanib (711 Ma)
Study area (740 Ma)
0 100 200 300 km
31°
27°
23°
29°
33°
37°
b
N
22° 45′
22° 44′
22° 40′
22° 34′
22° 30′
34° 56′
35°
35° 5′
35° 9′
W. Fadittal
G.Toboy
W. Euaktiubi
W. Sherefa El Gharbi
W.Seyet (HSZ)
G. Korab Kansi
1228
W.Wadhait
G.Direib
1145
W. Kamwib
Mt
65
70
75
80
0 1 2 3 4 5 6 7 8 9 10km
A
B
C
Dykes
Syn-tectonic granites
Pyroxene±Hb gabbros
Olivine gabbros/troctolite
Amphibole peridotites
Fe-Ti-bearing dunites
Intrusive rocks
Metasediments
Felsic to intermediate volcanic schists
Volcano-sedimentary association
Metavolcanics
Sheeted metadiabase dykes
Metagabbros
Serpentinites and their derivatives
Ophiolitic assemblage
Hornblendite dyke
Layering-strike and dip
Clinopyroxenite layer
Strike-slip fault
Mt Titanomagnetite ores
Thrust fault
Normal fault
c
Diagrammatic cross section
G. Korab Kansi
1200 m
800
400
Wadi deposit
Ilmenite
Hornblendite
Fe-Ti rich dunite
Olv. gabbro± troctolite
Pyx.hbl.gabbro
Pyroxene gabbros
Syn-tectonic granite (645-660 Ma)
A
B
C

parts of the intrusion at the contact with ophiolite sequences, and fine-grained gabbros are abundant here (Fig. 1b). The Korab Kansi intrusion is sometimes cut by vertical E-W trending basalt and andesite dykes that represent the final igneous activity in the studied area (Abdel-Gawad, 2002).

The Korab Kansi intrusion is differentiated into Fe-Ti-bearing dunites, amphibole peridotites, pyroxenites, troctolites (Fig. 2g), olivine gabbros, gabbronorites, pyroxene gabbros and hornblende pyroxene gabbros (Fig. 2). Dunites are layers or dykes sometimes associated with troctolite layers and hornblendite bands or lenses in the southern part of the intrusion (Fig. 1c). In addition, troctolites occurs as lenses or dykes and weather into spheroidal and onion-like boulders ranging in diameter from 20 cm to 2 m (Fig. 2g). Dunites and troctolites are enveloped by pyroxene gabbros that make up most of the intrusion. Pyroxenites are sometimes found as pockets and small dyke-like masses within pyroxene gabbros. They also occur as thin discontinuous layers in amphibole peridotites and olivine gabbros, near the contact with ophiolitic serpentinites (Fig. 1b). Olivine gabbros are brownish with a gradational contact with pyroxene gabbros and form an intrusive contact with serpntinites. They are found in the northwest of the mafic-ultramafic intrusion near the contact with ophiolitic serpentinites. Gabbroic rocks sometimes show small scale rhythmic layers of few mm to about 4 m (Fig. 2c, Abdel-Gawad, 2002). These layers are cumulates formed due to gravitational settling of crystals in the magma. In general, contacts between different gabbroic rocks are gradational.

The Korab Kansi intrusion hosts economic Fe-Ti deposits and Fe-Ti-rich dunite tabular layers in the southern part (Fig. 2a–b, h). These deposits and layers are concordant with the host layered mafic-ultramafic intrusion, and occur as multiple discontinuous parallel layers (Fig. 2b) in the form of dyke-like bodies associated with thin hornblendite bands within the gabbroic rocks (Fig. 2h). They sometimes occur in the apex of low-relief gabbroic hills. Troctolites also host the economic Fe-Ti oxides. Both dunites and troctolites are enveloped by pyroxene gabbros. Layering in the intrusion strike ~N-S and dip steeply east except in the east where the dip steeply west. The Fe-Ti oxide layers vary in width from 1.5 m to 5 m and can be traced NNW-SSE for around 600 m (Fig. 1b), where Makhlouf et al. (2008) traced Fe-Ti oxide-rich layers up to 2.5 km long.

3. Petrography of Korab Kansi mafic-ultramafic intrusion

The Korab Kansi intrusion consists of unmetamorphosed mafic-ultramafic igneous rocks comprising eight different petrographic varieties according to the modal abundance of constituent minerals determined by point counting.

Amphibole peridotites are highly sheared, and consist mainly of olivine (70–75 vol.%) and amphibole (15–20 vol.%) with minor plagioclase and opaques (Fig. 3b). Olivine ($Fo_{85.5-86}$) occurs as anhedral crystals with a few opaque inclusions. Cracks in olivines are mostly filled by fine-grained magnetite. Pargasitic amphiboles are found as intercumulus prismatic crystals, sometimes with small olivine inclusions (Fig. 3b). Opaques are represented by ilmenite, Al-spinel, pyrrhotite and pentlandite. Pyrrhotite is a common sulphide mineral with exsolved flame-like, lamellae and irregular grains of pentlandite. Al-spinel occurs as fine disseminated inclusions hosted in amphiboles and olivine.

Fe-Ti oxide-rich dunites are coarse-grained adcumulate rocks that consist mainly of various proportions of olivine, titanomagnetite, ilmenite with accessory sulphide phases. Olivine (40–70 vol.%) is mostly found as cumulus equigranular crystals (up to 3 × 2.5 mm, Fig. 3a). It has fresh cores ($Fo_{71.6-74.2}$), and is usually replaced by iddingsite at the rim (Fig. 3a). Some olivines are altered to serpentine and chlorite (Fig. 3a). The Fe-Ti oxides are represented by titanomagnetite and ilmenite found as intercumulus phases between cumulus olivines. All composite grains of magnetite and ilmenite show primary magmatic textures. They are associated with hornblendite bands (Fig. 1b).

Hornblendite bands are composed mainly of prismatic hornblende (70 vol.%) and Fe-Ti oxides (30%) with minor chlorite. The amphiboles in hornblendites are represented by pargasite and magnesiohornblende. The pargasite occurs as large plates with oriented needle-like or dust inclusions of ilmenite along the cleavage planes forming schiller structure. It is partially altered to fibrous magnesiohornblende along its peripheries. Chlorite is found as pockets consisting of fine fibrous aggregates and sometimes replaces pargasite along its cleavage planes.

Clinopyroxenites consist mainly of diopside with minor plagioclase (Fig. 3c). Al-spinel, ilmenite and magnetite are the main accessory minerals. Diopside (up to 90 vol.%) exists as granoblastic aggregates that mostly include fine plagioclase crystals (Fig. 3c). Small veinlets (2 mm width) of plagioclase cut the rock. Plagioclase exists as aggregates of equigranular and fine-grained crystals, showing a granoblastic texture. Ilmenite-magnetite trellis intergrowth is a common texture (Fig. 3d), and forms sharp contacts with the surrounding clinopyroxene.

Gabbroic rocks (more than 90% of total volume of intrusion) include troctolites, olivine gabbros, pyroxene gabbros, gabbronorites and pyroxene hornblende gabbros. They contain abundant titanomagnetite, ilmenite and magnetite with subordinate geothite and sulphides (Fig. 3f, g). Sulphides are represented by pyrrhotite, pentlandite, pyrite and chalcopyrite in decreasing order of abundance. Pyrrhotite with exsolved pentlandite is common in olivine gabbros, while alteration of pyrite into colloform goethite is common in gabbronorites.

Troctolites consist mainly of cumulus olivine (35–40 vol.%) and plagioclase (50–65 vol.%) with minor intercumulus clinopyroxene (Cpx), brown hornblende and opaques (<10 vol.%) (Fig. 3e, f). Some troctolite samples contain abundant Fe-Ti oxides, forming Fe-Ti oxide-rich troctolites (Fig. 3f). Troctolites show orthocumulate texture with coronas of orthopyroxene and/or pargasite around olivine (Fig. 3e). Olivine ($Fo_{68.9-70.5}$) is subhedral to anhedral and is generally fresh with partial alteration to iddingsite and serpentines along its cracks and rims. Plagioclase (An_{54-57}) occurs as cumulus subhedral prismatic crystals (1.5–3.5 mm), and few laths are enclosed within olivine and Cpx crystals (Fig. 3e). A few Cpx grains exist as intercumulus subhedral to anhedral crystals between olivine and plagioclase (Fig. 3e). The ilmenite occurs as composite and/or sandwich intergrowths between titanomagnetite that forms a sharp contact with cumulus olivine (Fig. 3f).

The fine-grained olivine gabbros at the contact with serpentinites are composed of fine olivine ($Fo_{77.7-78.7}$) grains, plagioclase, brown hornblende with minor amounts of Cpxs. Plagioclase ($An_{67.2-68.9}$) occurs as cumulus fine prismatic laths that are commonly enclosed in olivine, showing common poikilitic textures (Fig. 3g). Olivine crystals are mostly fresh and found as cumulus, fresh subrounded to rounded grains with sharp irregular contacts with other components. Cpxs and brown hornblende represent the intercumulus phases filling the irregular spaces between the cumulus phases.

Olivine gabbros are coarse-grained orthocumulate and composed mainly of cumulus olivine (Fo_{68-69}), plagioclase and minor orthopyroxene with few intercumulus augite grains. Chlorite is the main secondary mineral, while apatite and Fe-Ti oxides are accessory minerals. Several exsolution textures of ilmenite in titanomagnetite are observed (Fig. 3h). The schiller structure are observed in olivine gabbros (Fig. 3h), where augite is highly pitted with fine-grained magnetite giving rise a pronounced schiller structure .

Pyroxene gabbros are the most common rock type in the Korab Kansi intrusion, and consist mainly of cumulus plagioclase and intercumulus Cpx (augite) with minor brown hornblende and olivine

Fig. 1. Location and geological map of the Korab Kansi area, the SED of Egypt: **a**) Location map of the study area. **b**) Geological map of the Korab Kansi area (after Abdel-Gawad, 2002). **c**) Diagrammatic cross section of the Korab Kansi intrusion modified after the geologic map of Marsa Sha'ab quadrangle (GSE, 2002).

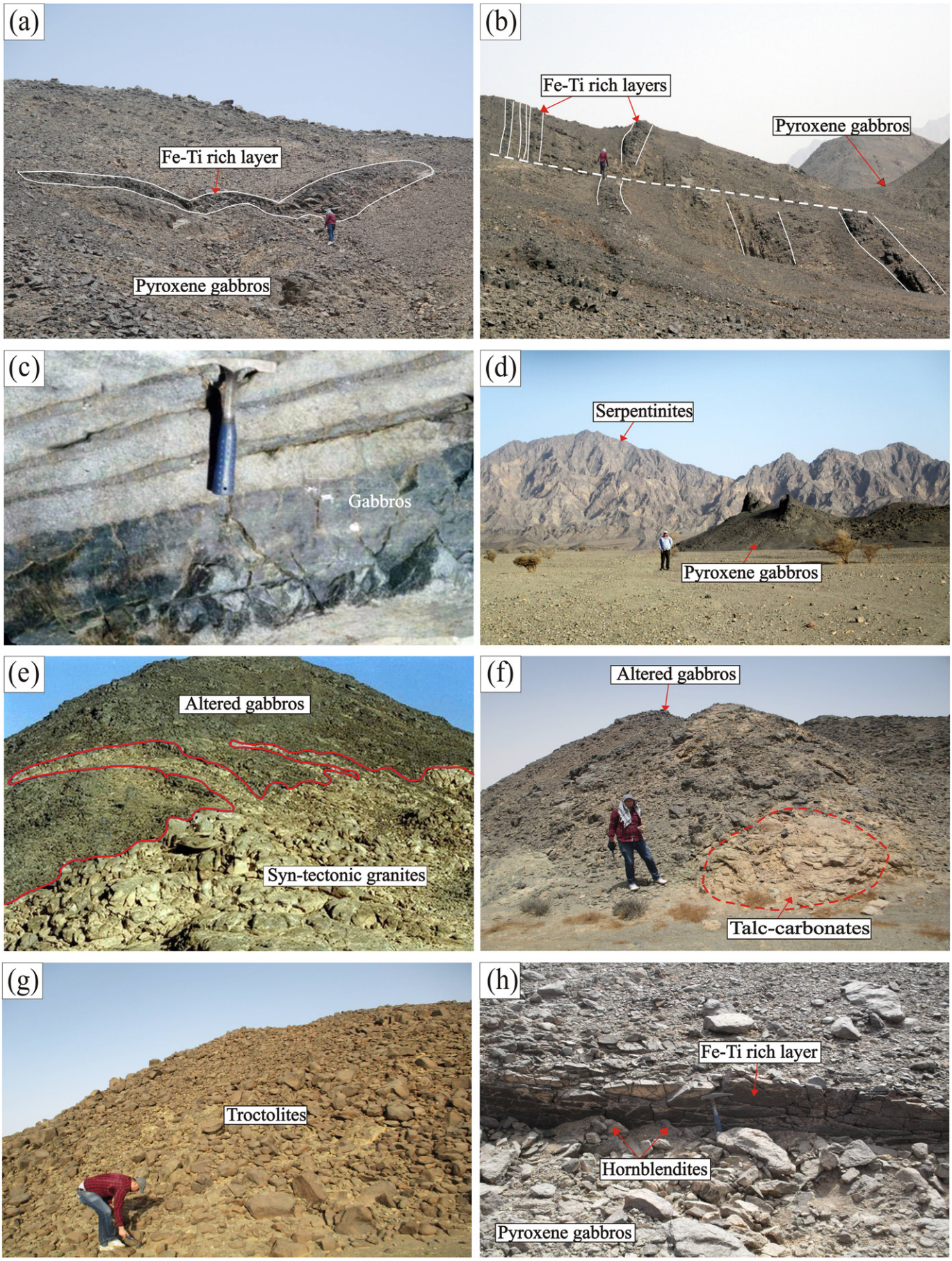
(a)
Fe-Ti rich layer
Pyroxene gabbros
(b)
Fe-Ti rich layers
Pyroxene gabbros
(c)
Gabbros
(d)
Serpentinites
Pyroxene gabbros
(e)
Altered gabbros
Syn-tectonic granites
(f)
Altered gabbros
Talc-carbonates
(g)
Troctolites
(h)
Fe-Ti rich layer
Hornblendites
Pyroxene gabbros

(Fig. 3i). Ophitic and sub-ophitic textures are dominant (Fig. 3i). Some samples are highly enriched with iron and titanium oxides. Ilmenite occurs mainly as composite grains with titanomagnetite, and sometimes as fine needles arranged along Cpx cleavage planes (Fig. 3j). Colloform goethite resulting from hydration of magnetite is common (Fig. 3j).

Pyroxene-hornblende gabbros consist mainly of plagioclase, brown hornblende, clinopyroxene (Cpx) and opaques (Fig. 3k). Their mineral shapes and habits are similar to those of troctolites. Olivine, plagioclase and Cpx crystals represent cumulus phases, and show orthocumulate textures. Brown hornblende is as intercumulus phase and/or as coronas surrounding the Cpx (Fig. 3k). Olivine is frequently rimmed by thin bands of orthopyroxene, forming corona textures. Some olivines are partially altered to iddingsite and greenish chlorite along margins and cracks. Plagioclase (An_{51-53}) occurs as subhedral tabular crystals (2.3–4.2 mm) or laths that are enclosed within olivine and pyroxene (Fig. 3k). Pyrite is the dominant sulphide mineral, and sometimes includes blebs of chalcopyrite.

Gabbronorites show orthocumulate to mesocumulate textures, and consist mainly of cumulus plagioclase and orthopyroxene (Opx) with intercumulus augite (Fig. 3l). Plagioclase (An_{53-55}) occurs as coarse columnar crystals that are sometimes ophitically and sub-ophitically enclosed by intercumulus augite. Opx occurs as prismatic crystals, showing a kink band texture. Augite occurs as large plates (1.8–3.25 mm), and exhibits schiller and corona structures.

4. Mineral chemistry

4.1. Major oxides

Major element composition of silicates, Fe-Ti oxides and sulphides (Table 1; Supplementary 2, 2) were analyzed using a JEOL JXA-8800 electron probe micro-analyzer (EPMA) at Kanazawa University (Japan). The analyses were conducted under 20 kV accelerating voltage, 20 nA beam current and 3 μm beam diameter. The data were corrected using a ZAF program (Bence and Albee, 1968). Cr-number (Cr#) and Mg-number (Mg#) of chromian spinel are Cr/(Cr + Al) and Mg/(Mg + Fe^{2+}) atomic ratios, respectively, but silicate Mg# is Mg/(Mg + Fe), where all Fe was assumed to be ferrous. Y_{Cr}, Y_{Al} and Y_{Fe} are the atomic ratios of Cr, Al and Fe^{3+}, respectively, to trivalent cations, (Cr + Al + Fe^{3+}).

Olivines have a wide range of compositions throughout the studied intrusion from peridotite to coarse-grained olivine gabbros. The forsterite content (Fo) ranges from 68 to 86 through the Korab Kansi intrusion (Fig. 4a; Supplementary 2). The most magnesian olivines are found in amphibole peridotites ($Fo_{85.5-86}$), fine-grained olivine gabbros ($Fo_{77.7-78.7}$), troctolites ($Fo_{68.9-70.5}$), and coarse olivine gabbros (Fo_{68-69}), respectively (Fig. 4a; Supplementary 2). Fo content of the investigated olivines resembles that of layered intruions in the SED of Egypt (Fig. 4a; Helmy and El Mahallawi, 2003; Abdel Halim et al., 2016) and the Bushveld complex in South Africa, but is more magnesian than olivine of the Skaergaard intrusion in east Greenland (Wager and Brown, 1967) (Supplementary 4a). The examined olivines contain low and variable contents of both NiO (bdl- 0.18 wt. %) and MnO (0.17–0.47 wt. %) (Table 1; Fig. 4a; Supplementary 2). Their NiO contents are similar to olivines in other Egyptian layered mafic intrusions (Fig. 4a), but lower than those of ophiolitic mantle olivines (Takahashi et al., 1987) including those in Egyptian ophiolites (Khedr and Arai, 2013, 2016a, 2017) (Fig. 4a).

Orthopyroxenes (Opxs) in olivine gabbros and gabbronorites are enstatite (En_{70-72}) with a narrow range of Mg# (0.73–0.77). They contain less Cr_2O_3 (<0.1 wt%), but more TiO_2 (0.3–0.7 wt%; Supplementary 2) than ophiolitic Opx from Egypt (Khedr and Arai, 2013, 2016a, 2017). Opx of gabbronorites contains slightly higher average SiO_2 (53.9 wt. %), Al_2O_3 (2.4 wt. %) and CaO (1.6 wt. %), but lower averages Mg# (0.74) and MnO (0.33 wt. %) than Opx of olivine gabbros (Table 1; Supplementary 2). Korab Kansi Opxs also exhibit similar Mg# and Al_2O_3 content with Opx of Genina Gharbia (Helmy et al., 2014) in the SED, and follows a low pressure differentiation trend (Fig. 4b). They are similar in Al_2O_3 and Mg# to Opx in boninite (Supplementary 4b).

Clinopyroxenes (Cpxs) are major constituents in most Korab Kansi lithologies. These Cpxs range in composition from augite (Wo_{39-44}) to diopside ($Wo_{43.8-48.3}$) with wide ranges of Mg# (0.57–0.95), following the Bushveld trend (Fig. 4c). They are very depleted in Cr_2O_3 (<0.1 wt%). The highest TiO_2 content (0.91–1.7 wt%) is recorded in the Cpxs of pyroxene gabbros that host Fe-Ti oxides layers (Supplementary 3). Cpx Al_2O_3 (1.0–6.7 wt%) and TiO_2 (0.3–1.7 wt%) contents show a good positive correlation, forming a systematic fractional-crystallization trend (Fig. 10c). Korab Kansi Cpxs have Al and Si contents similar to Cpxs of subalkaline mafic rocks with a few samples more similar to Cpxs of alkaline rocks (Le Bas, 1962; Fig. 10a). Korab Kansi Cpxs plot mainly in the fields of volcanic-arc basalts and island-arc basalts (Fig. 12), showing calc-alkaline to tholeiitic affinity (Le Bas, 1962; Leterrier et al., 1982; Fiala et al., 1975) (Fig. 10), permissive of an island arc setting (Fig. 12).

Korab Kansi amphiboles are mainly pargasite, magnesiohornblende and actinolite (Leake et al., 1997; Fig. 4d). Primary amphiboles are mainly pargasite with minor tschermakite, and contain more TiO_2 (up to 5.73 wt%), Al_2O_3 (19.17 wt%) and Na_2O (3.95 wt%) than the magnesiohornblende and actinolite that replace pyroxenes (Supplementary 2). Primary amphibole shows a wider range of Mg# (0.6-0.97) relative to secondary amphiboles (Mg#, 0.6–0.8) (Supplementary 2, 4c, d). The highest amphibole Mg# is recorded in peridotites (Mg# = 0.97 on average), while pyroxene-hornblende gabbros exhibit the lowest Mg#, i.e., amphibole Mg# = 0.64 on average. Hornblende Mg# correlates with the Mg# of coexisting olivines and pyroxenes. Amphibole coronas around Fe-Ti oxides minerals, Cpxs and olivines are mainly pargasite.

Korab Kansi plagioclase (Table 1) shows a wide compositional range from andesine to anorthite ($An_{40.9-93.6}$) (Fig. 4e). Anorthite ($An_{91.2-93.6}$) is only found as small veinlets traversing pyroxenites. Plagioclase in peridotites is bytownite ($An_{85.7-85.8}$). The studied troctolites, olivine gabbros and pyroxene gabbros include labradorite ($An_{50.6-68.9}$), while andesine ($An_{40.9-48.4}$) is only found in pyroxene-hornblende gabbros (Fig. 4e; Table 1; Supplementary 2).

Korab Kansi Fe-Ti oxides are mainly titanomagnetite, ilmenite and magnetite with subordinate amounts of goethite (Fig. 4f, Table 1; Supplementary 3). Korab Kansi ilmenite contains more TiO_2 (up to 57.2 wt%), MgO (7.8 wt%), MnO (up to 3.7 wt%) and V_2O_5 (3.62-4.45 wt%) and less FeO (35.3 wt%; Supplementary 3) compared to that in Skaergaard layered gabbros (Vincent and Phillips, 1954; Jang et al., 2001; Jang and Naslund, 2003). Korab Kansi ilmenite has low concentrations of minor elements such as ZnO (bdl-0.085 wt%) and CoO (0.05–0.1 wt%) (Supplementary 3). The high V_2O_5 (3.62-4.45 wt%) contents are recorded in both ilmenite and titanomagnetite (Supplementary 3), where TiO_2 content shows a positive correlation with V_2O_5, but anticorrelates with CoO (Supplementary 4e, f).

Korab Kansi magnetite ranges in composition from near end-member Fe_3O_4 to titanomagnetite with up to 17.9 wt% TiO_2 (Fig. 4f; Supplementary 3). It has variable amounts of MnO (0.03–1.4 wt%), Cr_2O_3 (bdl - 0.76 wt%), MgO (0.02 to 0.7 wt%), ZnO (bdl-0.29 wt%)

Fig. 2. Field photographs of the Korab Kansi mafic-ultramafic intrusion: **a**) Pinch and swell structure in the Fe-Ti oxide-rich dunite layers. **b**) Several Fe-Ti oxide-rich dunite layers displaced by fault. **c**) Small-scale rhythmic layers in the mafic-ultramafic intrusion, northern part of Gabal Korab Kansi (quotes from Abdel-Gawad, 2002). **d**) Sharp contact between intrusive gabbros and serpentinites. **e**) Sharp contact between gabbros and syn-tectonic granites, where granite arms extended in gabbros (quotes from Abdel-Gawad, 2002). **f**) Enclaves of talc-carbonate hosted in altered gabbros. **g**) Weathering surface of troctolites showing spheroidal boulders. **h**) Thin hornblendite bands showing a linear contact with Fe-Ti oxide-rich dunite layer hosted by pyroxene gabbros.

and CoO (0.05–0.099 wt%; Supplementary 3). Magnetite ulvospinel content is below 2.42 mole% (Supplementary 3) according to Stromer (1983), consistent with rare fine trellis intergrowth of ulvospinel in magnetite. Sulphides are less abundant than Fe-Ti oxides, mainly pyrrhotite, pentlandite, chalcopyrite and pyrite (Supplementary 3). High concentrations of Au (0.09-0.5 wt%) and Mo (0.37-0.8 wt%) are

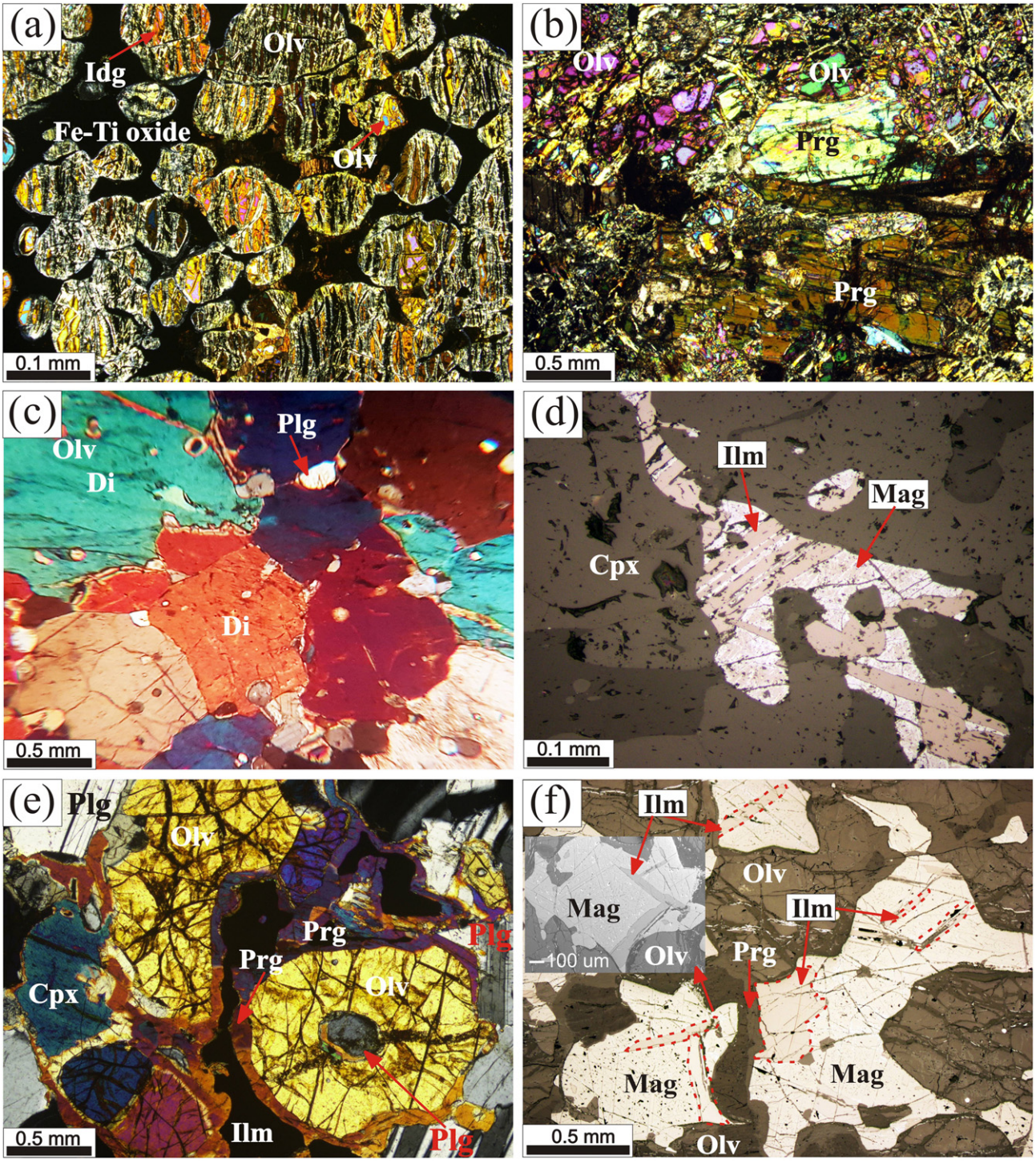

Fig. 3. Photomicrographs of Fe-Ti oxides-rich mafic-ultramafic rocks from the Korab Kansi intrusion. All photos were taken under crossed polarized light except **d**, **f**, **h** and **j** taken under reflected light. **a**) Rounded cumulus olivine (Olv) crystals partially altered to iddingsite (Idg) with intercumulus Fe-Ti oxides in Fe-Ti oxide-rich dunites. **b**) Prismatic pargasite (Prg) crystals in contact with highly fractured olivines in amphibole peridotites. **c**) Granoblastic aggregates of diopside (Di) enclosing fine plagioclase (Plg) crystals in pyroxenites. **d**) Ilmenite (Ilm)- magnetite (Mag) trellis intergrowth (magmatic texture) with sharp contact with pyroxene (Cpx) in pyroxenites. **e**). Thin rims of pargasite surrounding both olivine and ilmenite, forming corona structure in troctolites. **f**). Composite and sandwich intergrowths between ilmenite (Ilm) and magnetite (Mag), where one grain of ilmenite embedded in magnetite was taken as back scattered electron image (troctolites). **g**). Poikilitic olivine (Olv) sieved by plagioclase in fine-grained olivine gabbros. **h**). Ilmenite (Ilm)-magnetite (Mag) banded intergrowth in olivine gabbros. .**i**) Plagioclase (Plg) crystals ophitically enclosed in large clinopyroxene (Cpx) surrounded by pargasite (Prg) corona at the contact in pyroxene gabbros. **j**) Colloform texture of goethite (Gth) and fine ilmenite needles (Ilm) arranged along the cleavage planes of clinopyroxene (Cpx) in pyroxene gabbros. **k)** Corona of pargasite (Prg) at the contact between plagioclase (Plg) and clinopyroxene in pyroxene-hornblende gabbros. **l**) Cracked orthopyroxene (Opx) crystals in contact with plagioclase (Plg) and pargasite corona around titanomagnetite (Ti-Mag) in gabbronorites.

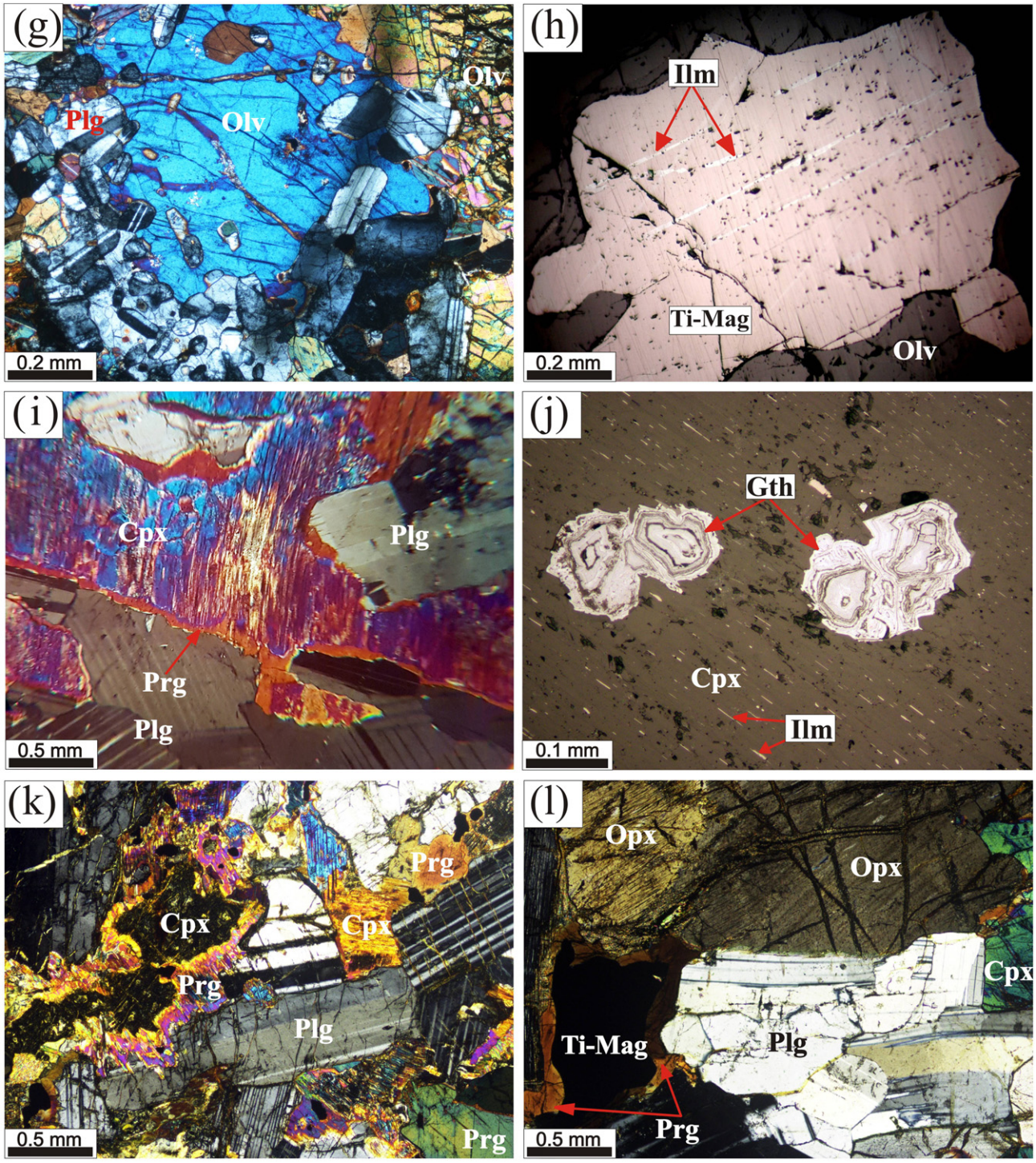

Fig. 3 (*continued*).

recorded in all sulphide minerals, while pyrite is rich in Co (3.3-6.4 wt%) (Supplementary 3). The pyrite Co/Ni ratio is >1, similar to volcanic-associated pyrites (Loftus-Hills and Solomon, 1967).

4.2. In-situ trace elements of silicates

The concentrations of trace elements in clinopyroxenes, orthopyroxenes, amphiboles and plagioclase from Korab Kansi mafic-ultramafic rocks (Table 2; Figs. 5, 6) were determined in-situ by laser-ablation (193 nm ArF excimer: MicroLas GeoLas Q-plus)-inductively coupled plasma mass spectrometry (Agilent 7500 S) (LA–ICP–MS) at Kanazawa University, Japan. Analyses were done by ablating 40-μm diameter spots at 6 Hz with an energy density of 8 J/cm^2 per pulse. The precision or reproducibility is better than <5% for most elements, except Sc, Cr and Ni for which it is better than <10%.

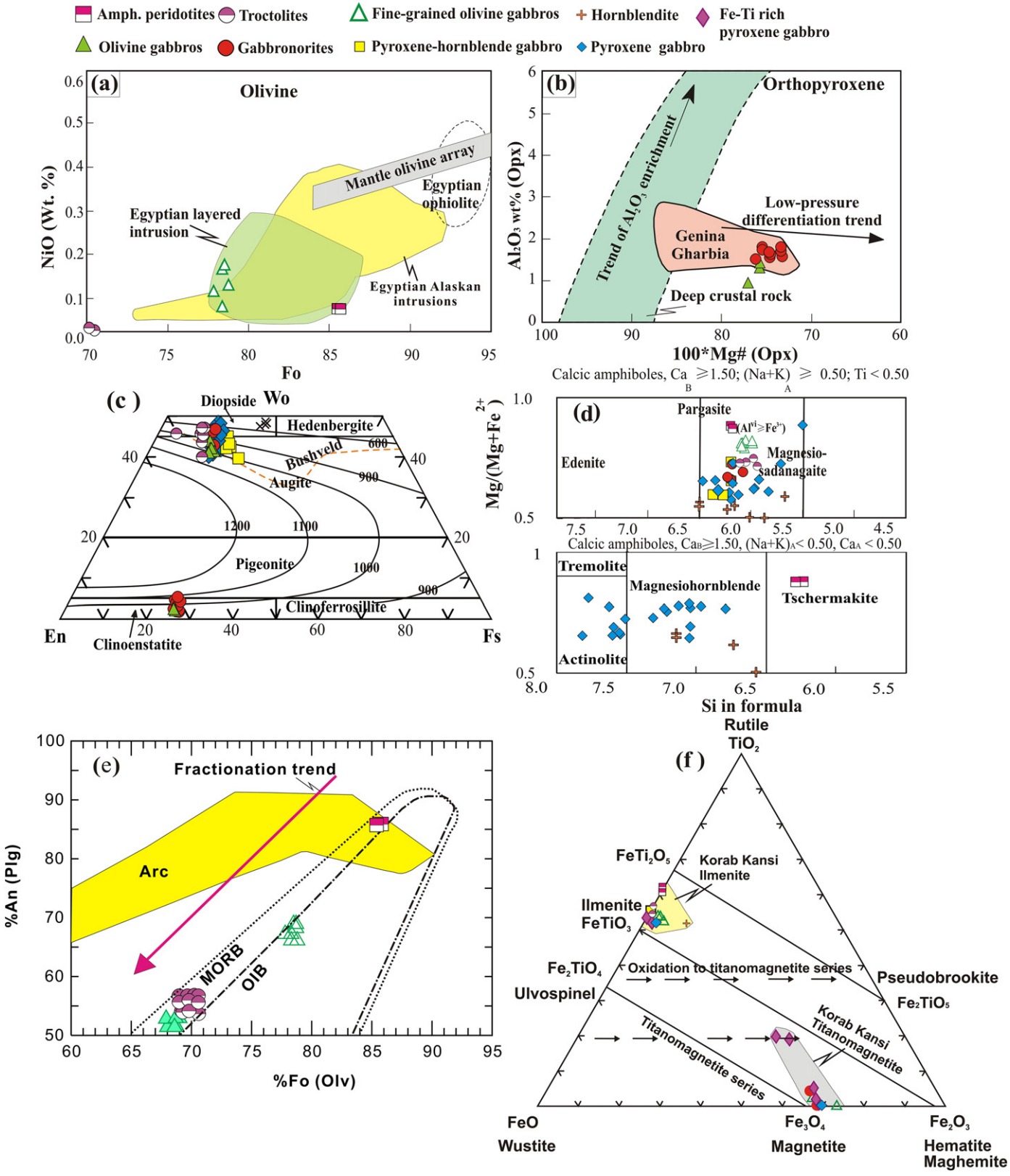

Fig. 4. Chemistry of olivines, pyroxenes, amphiboles, plagioclase and Fe-Ti oxides in the Korab Kansi intrusion. **a**) Variation diagram of NiO (wt%) and Fo content of the olivines. The field of Egyptian layered intrusion (Azer et al., 2016; Essawy et al., 1997; Khudeir, 1995), Egyptian ophiolite (Khedr and Arai, 2013, 2016a, 2017) and Egyptian Alaskan intrusions (Helmy and Mogessie, 2001; Helmy et al., 2014; Khedr and Arai, 2016b) are used for comparison. The ophiolitic mantle olivine field is after Takahashi et al. (1987). **b**) Variation diagram of Al_2O_3 (wt%) vs. 100*Mg# of Opxs. Fields of deep crustal rocks (DeBari and Coleman, 1989) and Genina Gharbia Alaskan rocks (Helmy et al., 2014) are used for comparison. **c**) Wo-En-Fs nomenclature diagram of Cpx (Morimoto et al., 1988). The isothermal lines are after LindsleyStromer Jr. (1983) and the dotted orange line indicates the Bushveld trend (Atkin, 1969). **d**) Amphiboles nomenclature diagrams (Leake et al., 1997). **e**) The coexisting olivine forsterite (Olv Fo) and plagioclase anorthite (Plg An) compositions. The fields for arc basalts and fields for MORB and OIB are after Stern et al. (2006). **f**) FeO-TiO_2-Fe_2O_3 triangular diagram of Fe-Ti oxides showing oxides mainly titanomagnetite, ilmenite, and magnetite.

Table 1
Representative microprobe analyses of olivine, clinopyroxene, orthopyroxene, amphibole, plagioclase and Fe-Ti oxides from Korab Kansi mafic-ultramafic rocks.

Rock name	Peridotites				Pyroxenites			Troctolites						Olivine gabbros						Fine-olv gbs	
Sample no.	Sn.12				Sn.9			Kn.41						Kn.9						Sn. 16	
Mineral	Olv	Prg	Plg	Ilm	Cpx	Plg	Mag	Olv	Cpx	Plg	Prg	Ilm	Gt	Olv	Cpx	Opx	Plg	Mag	Ilm	Olv	Prg
SiO_2	41.02	44.85	47.50	0.00	47.83	45.07	0.86	38.32	51.07	54.32	42.05	0.00	12.60	37.51	50.36	52.92	54.35	0.86	0.00	38.77	41.94
TiO_2	0.00	2.06	0.05	57.17	1.57	0.00	0.90	0.00	1.17	0.05	2.40	54.65	0.00	0.00	0.88	0.33	0.00	0.90	52.52	0.00	5.44
Al_2O_3	0.00	14.60	34.43	0.02	6.74	35.19	0.74	0.00	4.43	29.34	14.95	0.02	0.09	0.00	3.63	2.16	28.50	0.74	0.07	0.00	13.22
Cr_2O_3	0.00	0.00	0.11	0.05	0.00	0.00	0.47	0.00	0.06	0.00	0.00	0.00	0.00	0.00	0.00	0.05	0.18	0.47	0.00	0.00	0.62
FeO^t	13.73	4.45	0.11	35.43	13.54	0.46	86.15	26.88	5.74	0.11	9.21	41.98	62.26	28.10	7.65	16.11	0.00	86.15	45.10	20.20	6.93
MnO	0.27	0.08	0.00	0.52	0.23	0.00	0.03	0.36	0.15	0.00	0.15	0.60	0.02	0.47	0.24	0.46	0.00	0.03	0.58	0.30	0.09
MgO	46.03	17.93	0.02	7.79	9.13	0.06	0.28	34.88	15.29	0.01	13.72	3.27	1.96	35.21	14.77	26.18	0.00	0.28	1.10	41.61	14.47
CaO	0.00	12.03	18.06	0.00	21.91	18.55	0.00	0.00	21.77	12.05	11.70	0.00	0.54	0.06	21.10	1.12	10.94	0.00	0.00	0.01	11.28
Na_2O	0.00	2.87	1.66	0.00	0.24	0.82	0.00	0.01	0.73	5.04	2.66	0.00	0.12	0.08	0.47	0.00	5.32	0.00	0.06	0.02	3.14
K_2O	0.00	0.13	0.00	0.00	0.00	0.06	0.00	0.00	0.01	0.04	0.86	0.00	0.11	0.00	0.00	0.00	0.08	0.00	0.00	0.01	0.45
NiO	0.07	0.02	0.00	0.00	0.04	0.00	0.00	0.06	0.00	0.00	0.00	0.00	0.06	0.00	0.00	0.00	0.00	0.00	0.00	0.17	0.03
Total	101.12	99.03	101.93	100.98	101.23	100.21	89.43	100.51	100.42	100.96	97.70	100.51	77.75	101.43	99.10	99.38	99.37	89.43	99.43	101.07	97.59
Wo					47.87				44.48						43.40	2.22					
En					27.76				43.48						42.27	72.21					
Fo	85.43							69.53						68.97						78.35	
An			85.75			92.27				56.82							52.95				
Mg#	0.86	0.98			0.63			0.70	0.89		0.77			0.69	0.78	0.76				0.79	0.79

Rock name	Fine-olv gbs		Gabbronorites							Pyroxene gabbros			Fe-Ti oxide rich pyroxene gabbros						Pyroxene-hornblende gabbros			
Sample no.	Sn. 16r		Sn. 4							Sn. 2			Kn. 2						Sn.10			
Mineral	Plg	Gt	Cpx	Opx	Plg	Prg	Ti-Mag	Ilm	Gt	Cpx	Plg	Ilm	Cpx	Plg	Prg	Mag	Ti-Mag	Ilm	Cpx	Prg	Plg	Ilm
SiO_2	51.63	5.29	51.56	54.55	54.68	42.49	0.00	0.00	2.65	52.65	54.57	0.00	50.71	55.46	41.57	0.59	0.06	0.00	50.91	42.39	57.94	0.00
TiO_2	0.09	0.01	0.95	0.36	0.01	3.75	4.20	52.63	0.00	0.27	0.00	53.17	1.39	0.07	0.51	0.82	17.64	53.31	1.03	4.05	0.13	54.16
Al_2O_3	31.70	0.00	3.73	2.28	28.78	13.14	3.25	0.00	0.08	1.21	28.07	0.00	3.69	28.63	15.68	0.21	4.14	0.02	4.08	11.88	26.83	0.00
Cr_2O_3	0.00	65.74	0.00	0.12	0.00	0.04	1.25	0.00	0.00	0.00	0.00	0.00	0.00	0.00	0.00	0.02	0.00	0.00	0.00	0.00	0.00	0.00
FeO^a	0.07	0.30	7.09	16.08	0.09	9.67	81.52	43.25	65.96	8.29	0.06	43.95	9.09	0.66	16.26	87.22	69.58	45.69	10.51	15.01	0.09	44.56
MnO	0.00	2.49	0.20	0.33	0.02	0.12	0.51	3.73	0.00	0.21	0.00	0.73	0.18	0.03	0.19	0.04	1.45	0.70	0.30	0.20	0.00	0.67
MgO	0.03	0.19	13.91	26.45	0.00	13.61	0.70	0.25	0.19	14.33	0.00	0.68	13.95	0.08	9.37	0.23	0.12	0.27	12.98	10.63	0.00	0.22
CaO	13.85	0.03	22.14	1.20	11.34	11.63	0.00	0.00	2.13	22.21	10.66	0.00	20.41	11.30	10.95	0.00	0.00	0.00	19.51	10.58	8.77	0.00
Na_2O	3.69	0.00	0.60	0.03	5.12	2.18	0.00	0.00	0.13	0.24	5.49	0.00	0.47	4.64	2.91	0.02	0.05	0.02	1.04	2.73	6.61	0.01
K_2O	0.07	0.00	0.00	0.00	0.07	0.67	0.00	0.00	0.01	0.00	0.08	0.00	0.00	0.44	0.17	0.00	0.00	0.00	0.08	0.75	0.07	0.00
NiO	0.02	0.22	0.00	0.00	0.00	0.00	0.03	0.02	0.42	0.00	0.00	0.00	0.00	0.02	0.00	0.00	0.00	0.00	0.00	0.00	0.00	0.00
Total	101.16	74.26	100.18	101.38	100.10	97.30	91.44	99.88	71.57	99.40	98.93	98.52	99.88	101.32	97.61	89.14	93.02	100.01	100.43	98.25	100.42	99.63
Wo			45.88	2.35						45.13			42.55						40.79			
En			40.10	72.34						40.53			40.49						37.75			
An	67.20				54.86						51.53			55.90							42.16	
Mg#			0.80	0.75		0.75				0.76			0.80		0.59				0.74	0.59		

Total iron as FeOt; Fine-olv gbs: fine-grain olivine gabbros; Olv: olivine; Prg: pargasite; Plg: plagioclase; Ilm: ilmenite; Cpx: clinopyroxene; Mag: magnetite; Ilm: ilmenite; Gt: geothite; Opx: orthopyroxene; Wo = Ca/(Ca + Mg + Fe + Mn); En = Mg/(Mg + Ca + Fe + Mn); Fo = 100 * Mg/(Mg+Fe); An = Ca/(Ca + Na); Mg# = Mg/(Mg + Fe) atomic ratio.

Table 2
Trace elements (ppm) of clinopyroxene, orthopyroxene, amphibole and plagioclase in Korab Kansi mafic–ultramafic intrusion.

Rock type	Pyroxenites					Troctolites				Fe-Ti rich pyroxene gabbros				Gabbronorites					Pyroxene-hornblende gabbros					Hornblendites		
Mineral	Cpx				Plg	Cpx		Amph		Cpx			Plg	Cpx		Opx		Amph	Cpx			Amph	Plg	Amph		
Sample no.	Sn-9					Kn.41				Kn.2				Sn.4					Sn.10					Kn.7		
Trace elements (ppm)																										
Li	7.78	6.36	7.34	7.58	bdl	2.25	2.07	1.10	0.79	5.89	7.97	7.00	3.40	3.02	3.31	1.30	1.25	0.76	2.46	9.71	11.62	0.94	bdl	3.68	0.58	7.52
B	6.90	6.82	7.96	6.26	9.15	12.18	12.36	13.14	14.53	15.64	15.69	12.23	15.59	11.41	10.39	10.67	10.61	21.04	9.03	6.48	12.89	12.20	11.47	7.39	4.65	7.12
Sc	54.87	48.19	48.14	50.12	0.97	96.89	98.06	69.85	62.87	104.79	80.44	84.54	1.64	94.87	105.00	34.99	34.87	83.52	59.31	107.09	119.09	106.14	1.47	25.71	8.01	4.53
Ti	10,124	7,727	8,043	8,409	140.56	5,836	6,170	13,406	17,201	9,833	5,453	7,134	618.40	5,886	7,659	2,650	2,648	26,361	22,545	4,185	5,349	22,914	685.40	4,511	1,217	1,802
V	452.46	413.77	402.13	447.71	1.21	397.52	423.52	405.98	1,145	313.09	272.26	244.76	1.82	298.37	349.95	159.98	154.18	649.64	843.88	612.30	575.86	1,458	4.88	1,126	461.46	162.82
Cr	103.06	102.27	86.00	110.91	bdl	244.58	639.07	205.83	534.60	6.07	15.45	4.09	bdl	146.87	196.55	599.02	594.12	629.98	74.04	185.99	137.98	387.41	bdl	219.29	331.43	2.59
Co	70.69	73.99	74.11	75.29	0.50	41.62	42.58	55.82	54.89	51.98	59.62	57.00	0.66	43.06	44.75	98.23	95.07	70.17	66.02	45.66	38.64	55.94	0.41	74.02	62.25	73.40
Ni	73.40	73.31	73.80	77.53	bdl	60.04	63.26	105.39	103.38	75.22	117.09	77.55	bdl	61.30	57.36	121.02	118.82	130.24	117.23	71.86	83.00	143.29	1.46	215.33	201.12	146.44
As	bdl	bdl	bdl	bdl	bdl	bdl	bdl	bdl	bdl	0.41	0.34	0.38	bdl	bdl	bdl	bdl	bdl	0.49	bdl	bdl	0.48	0.61	bdl	bdl	bdl	bdl
Rb	bdl	0.03	0.04	bdl	4.26	0.06	0.07	1.38	1.54	bdl	0.09	0.08	11.20	bdl	bdl	0.06	0.05	3.19	3.51	0.16	0.47	2.56	0.45	0.40	0.22	0.22
Sr	93.42	82.85	80.72	64.69	1,069	34.79	38.83	168.42	185.24	54.67	37.79	45.87	1,200	27.30	27.01	0.62	0.59	185.98	146.11	22.80	28.56	154.15	653.46	25.10	18.96	28.89
Y	26.69	25.40	25.37	29.24	1.93	28.35	21.89	28.17	16.59	23.21	14.09	19.68	0.47	30.76	31.08	3.71	3.69	37.62	24.35	34.79	38.63	48.77	0.77	10.58	1.54	4.16
Zr	61.60	59.00	58.16	65.92	0.02	52.93	46.58	49.65	65.67	48.17	21.17	30.49	0.04	62.17	45.42	4.21	4.15	70.65	95.64	53.52	63.04	98.17	4.28	7.55	3.13	6.13
Nb	0.02	0.05	0.06	0.08	0.00	0.05	0.12	2.83	3.80	0.14	0.06	0.10	bdl	0.02	0.02	bdl	bdl	3.30	2.26	0.02	0.06	2.63	0.08	0.49	0.18	0.33
Cs	bdl	bdl	bdl	bdl	0.18	bdl	bdl	bdl	bdl	bdl	0.03	bdl	1.08	bdl	bdl	0.03	0.03	0.07	0.06	bdl	0.06	bdl	bdl	0.29	0.02	0.09
Ba	0.13	0.10	0.09	0.57	63.20	3.40	4.35	57.02	57.15	bdl	0.90	0.53	228.97	0.06	bdl	0.06	0.05	67.44	56.67	2.63	4.57	59.55	92.92	7.12	1.15	6.33
La	0.98	1.23	1.33	1.54	1.02	1.12	0.98	2.47	2.42	2.97	1.59	2.20	1.97	1.63	1.77	0.03	0.03	3.54	4.81	1.43	1.98	4.26	1.69	0.97	0.25	0.80
Ce	5.13	6.42	6.58	7.88	2.76	7.16	5.67	12.74	11.13	14.43	7.78	10.73	3.61	9.31	9.89	0.23	0.20	17.61	19.71	9.05	9.42	22.14	3.70	5.67	1.52	4.41
Pr	1.04	1.20	1.22	1.46	0.35	1.57	1.21	2.45	1.94	2.79	1.49	2.03	0.34	1.86	1.90	0.04	0.04	3.20	2.99	1.94	2.05	3.97	0.39	1.10	0.26	0.77
Nd	6.46	7.10	7.09	8.39	1.50	10.62	7.86	14.96	10.36	16.66	8.78	12.62	1.33	11.46	11.49	0.28	0.24	18.16	14.58	12.67	13.85	23.15	1.58	6.13	1.17	3.73
Sm	2.64	2.71	2.75	3.14	0.38	4.23	3.19	5.02	2.97	5.52	3.04	4.36	0.17	4.32	4.33	0.13	0.13	5.77	3.82	4.99	5.67	8.00	0.28	1.88	0.28	0.76
Eu	0.90	0.88	0.89	1.02	0.77	1.06	0.90	1.88	1.47	1.75	1.00	1.37	0.61	1.39	1.42	0.06	0.06	2.18	2.37	1.00	1.25	2.27	1.23	0.80	0.40	0.67
Gd	3.66	3.66	3.64	4.24	0.36	5.36	4.11	5.72	3.08	5.91	3.38	4.84	0.15	5.43	5.48	0.28	0.26	6.64	3.86	6.37	7.20	9.01	0.22	2.01	0.28	0.65
Tb	0.67	0.68	0.66	0.78	0.05	0.89	0.69	0.90	0.48	0.88	0.52	0.72	0.01	0.93	0.93	0.06	0.05	1.07	0.65	1.07	1.21	1.46	0.03	0.33	0.04	0.11
Dy	4.93	4.80	4.73	5.52	0.33	5.96	4.55	5.80	3.14	5.55	3.29	4.45	0.09	6.32	6.27	0.58	0.55	7.46	4.39	7.32	8.21	9.81	0.17	2.18	0.29	0.69
Ho	1.00	1.02	0.99	1.14	0.06	1.18	0.91	1.13	0.62	1.02	0.58	0.82	0.02	1.20	1.26	0.14	0.13	1.51	0.93	1.43	1.64	1.91	0.02	0.43	0.06	0.14
Er	3.01	2.90	2.89	3.37	0.15	3.11	2.47	3.04	1.90	2.52	1.55	2.13	0.07	3.41	3.46	0.51	0.51	4.20	2.81	3.99	4.38	5.20	0.08	1.14	0.17	0.44
Tm	0.45	0.43	0.43	0.52	0.02	0.43	0.33	0.44	0.30	0.32	0.21	0.27	bdl	0.47	0.48	0.10	0.10	0.58	0.44	0.56	0.61	0.71	bdl	0.16	0.03	0.08
Yb	3.10	3.04	3.07	3.62	0.10	2.77	2.22	2.93	2.18	2.08	1.42	1.77	0.06	3.06	3.21	0.81	0.80	4.01	3.36	3.71	3.92	4.87	bdl	1.06	0.21	0.58
Lu	0.44	0.42	0.45	0.50	0.02	0.37	0.29	0.42	0.32	0.28	0.19	0.24	bdl	0.42	0.43	0.14	0.14	0.52	0.51	0.50	0.54	0.61	bdl	0.16	0.03	0.09
Hf	1.96	1.91	1.86	2.09	bdl	2.30	1.89	1.67	1.77	2.42	1.03	1.49	bdl	2.33	1.61	0.16	0.15	2.25	2.11	1.87	2.45	3.63	0.12	0.40	0.13	0.15
Ta	bdl	0.02	0.01	0.02	bdl	0.01	bdl	0.18	0.18	0.03	bdl	0.02	bdl	bdl	bdl	bdl	bdl	0.19	0.15	0.00	0.00	0.16	bdl	0.05	0.02	0.02
Pb	0.20	0.24	0.25	0.20	0.68	0.08	0.10	0.28	0.38	0.11	0.50	1.34	1.91	0.16	0.18	bdl	bdl	0.65	0.56	bdl	0.66	0.69	1.11	0.22	0.12	0.22
Th	bdl	bdl	bdl	0.02	bdl	0.05	0.05	0.10	0.09	0.02	0.04	0.02	bdl	0.07	0.12	bdl	bdl	0.12	0.17	0.10	0.09	0.10	0.04	0.06	0.01	0.02
U	bdl	bdl	0.01	0.01	bdl	0.02	0.02	0.04	0.04	bdl	0.02	bdl	bdl	0.03	0.05	bdl	bdl	0.07	0.07	0.02	0.02	0.04	bdl	0.03	bdl	0.02
Sum REE	34.39	36.48	36.70	43.13	7.87	45.83	35.37	59.90	42.31	62.69	34.82	48.55	8.43	51.22	52.33	3.40	3.24	76.45	65.23	56.05	61.92	97.37	9.38	24.01	4.99	13.92
(La/Lu)N	0.23	0.30	0.31	0.32	6.41	0.32	0.35	0.62	0.80	1.12	0.88	0.95	0.00	0.41	0.42	0.02	0.02	0.70	0.98	0.30	0.38	0.73	0.00	0.64	0.79	0.90

bdl: below detection limits; Cpx: clinopyroxene; Plg: plagioclase; Amph: amphibole; Opx: orthopyroxene

Cpx rare earth elements (REE) were normalized to chondrite (CI) and the primitive mantle (PM) after McDonough and Sun (1995) (Fig. 5a, b). Cpxs in pyroxenites are lower in total REE abundances (ΣREEs: 37.7 ppm) than those in pyroxene-hornblende gabbros (ΣREEs: 61.1 ppm; Table 2). REE patterns of Cpxs (Fig. 5a) show a convex upward shape resulting from strong depletion of light rare earth elements (LREE: La-Nd) relative to both middle REE (Sm, Eu, Gd) and heavy rare earth elements (HREE: Tb-Lu), like Cpx REE patterns in layered mafic-ultramafic rocks of the Motaghairat intrusion in the SED of Egypt (Abdel Halim et al., 2016), tholeiitic lavas from Kilauea, Hawaii (Norman et al., 2005) and ferropicrites and picritic ferrobasaltic lavas from Lalibela, Ethiopian large igneous province (Desta et al., 2014). They slightly differ in shape compared with those of Alaskan Dahanib gabbros (Fig. 5a). Small negative Eu anomalies are recorded in most Cpx, which can be attributed to Eu incorporation in coexisting plagioclase. Primitive mantle-normalized trace-element patterns of Cpxs exhibit negative anomalies for Ba, Nb, Ta, Pb, Cr, Ni, Sr and Zr (Fig. 5b). The depletion of HFSE (e.g. Nb, Ta and Zr) plus Pb and Cr in the Korab Kansi Cpxs indictates the coexistence of accessory phases especially ilmenite and magnetite, while Sr, Ba and Eu depletion reflects coexisting plagioclase. Cpxs are poor in Ni (Fig. 5b), but are rich in some fluid-mobile elements (B, and Li, 2-80 times PM; Fig. 5b).

The chondrite-normalized REE pattern of Opx in gabbronorites shows steeply inclined patterns with strong depletion of LREE relative to HREE $(La/Lu)_N = 0.02$ (Fig. 5c), similar to Opx REE patterns of Motaghairat pyroxenites (Abdel Halim et al., 2016) (Fig. 5c). The primitive mantle (PM)-normalized trace element patterns of orthopyroxene display enrichment of B, Li, Cs and Ti (>0.9 times PM), but depletion in Ba, Th, U, Nb, Ta and Sr (<0.06 times PM) relative to adjacent elements (Fig. 5d). Amphibole REE concentrations are low in troctolite (ΣREEs = 51 ppm, on average) relative to that in pyroxene-hornblende gabbros (ΣREEs = 97.4 ppm) (Table 2). The REE contents of corona amphiboles rimming Cpx (ΣREEs = 59.9 ppm) are higher than those of amphiboles rimming ilmenite (ΣREEs = 42.3 ppm) in troctolites. The chondrite (CI)-normalized REEs patterns of amphiboles from gabbroic rocks are similar to those (ΣREEs = 14.3 ppm, on average) of hornblendites (Fig. 6a). These amphiboles show convex upward REE-patterns from Sm to La and nearly flat HREE patterns (Fig. 6a).

The multi-element patterns of amphiboles in the gabbroic rocks are highly enriched in B, Cs, Ba, Nb, Ce, Pr, Nd and V (>7.0 times PM), but depleted in U, Th, Pb, Zr and Hf (<7.0 times PM) relative to adjacent elements (Fig. 6b). On the other hand, the amphibole in hornblendites is enriched in B, Cs, Ce, Pr, Sm and Eu relative to surrounding elements (Fig. 6b). All Korab Kansi amphiboles are depleted in Cr, Ni, Hf, Zr and Pb (Fig. 6b). The plagioclases in pyroxenites, pyroxene gabbros and pyroxene-hornblende gabbros are rich in LREE relative to HREE with a pronounced positive Eu anomaly (Fig. 6c). Their multi-element patterns show variable enrichment of Ba, Pb, Sr and B (Fig. 6d).

5. Whole-rock chemistry

Major elements and selected trace elements (Cr, Ni, V) of whole rocks were analyzed with a Bruker Pioneer S4 X-ray fluorescence (XRF) spectrometer at the NAWI Graz Geocenter - Institute of Earth Sciences, Petrology and Geochemistry, University of Graz, Austria. Samples were prepared as fused glass discs using 1 gram of dried powdered rock material and 7 gram of di-lithium tetraborate (Fluxana). The glass discs were fused at about 1300 °C using a semi-automatic VAA-2 fusion machine from HD Electronic. Loss on ignition (LOI) was determined by heating the powdered rock material to 1025 °C for more than 1 h. About 80 international reference materials were used for calibrating the Bruker Pioneer S4. For quality control, the international reference materials BNV-1, GSP-2, MGL-GAS and OPY-1 were measured as external standards.

Trace and rare earth elements (REE) were determined by ICP-MS. Samples were dissolved at the clean room facility of the NAWI Graz Geocenter - Institute of Earth Sciences, Petrology and Geochemistry, University of Graz by using approximately 50 mg of sample powder

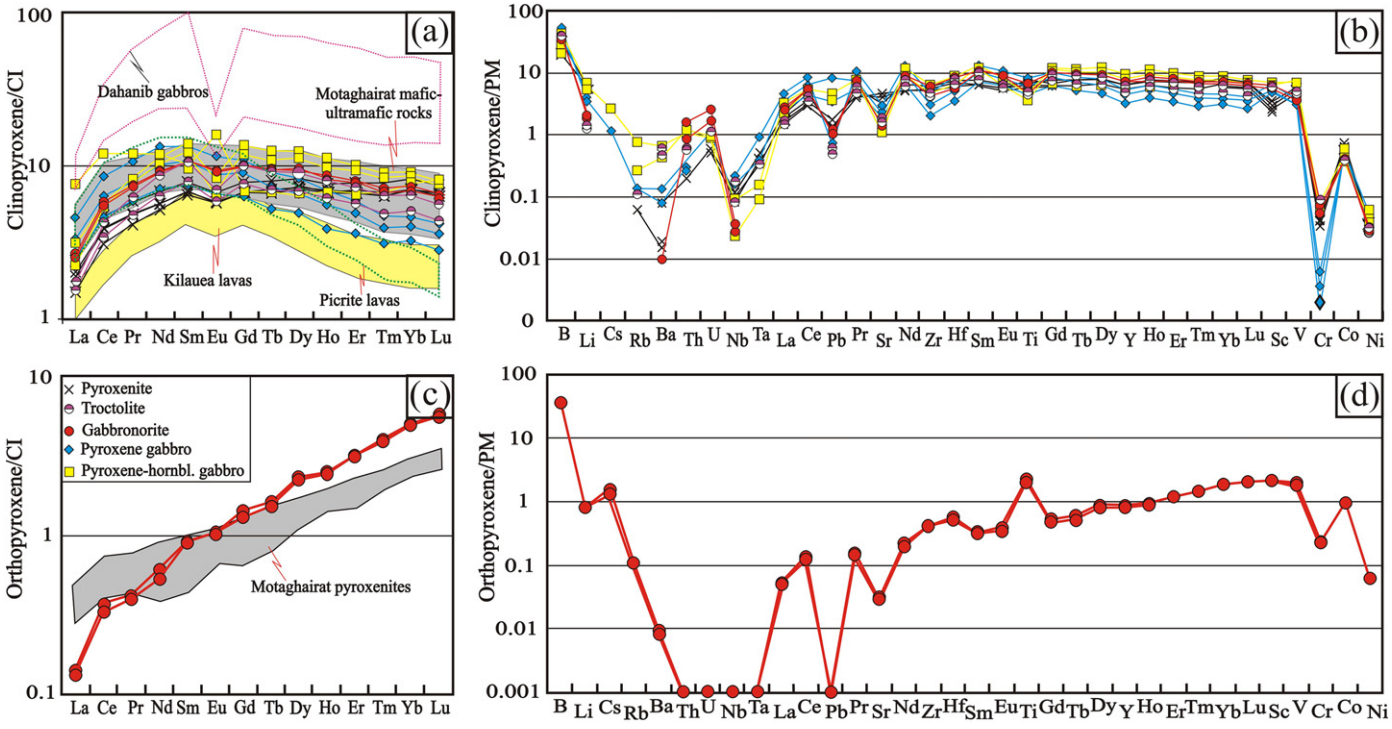

Fig. 5. In-situ trace and rare earth elements of Korab Kansi pyroxenes. **a**) Chondrite (C1)-normalized REEs patterns of clinopyroxenes in the studied mafic-ultramafic rocks compared with those from the Motaghairat mafic-ultramafic intrusion (Abdel Halim et al., 2016), tholeiitic lavas from Kilauea volcano in Hawaii (Norman et al., 2005), ferropicrites and picritic ferrobasaltic lavas from Lalibela area, Ethiopian large igneous province (Desta et al., 2014) and Dahanib Alaskan-type gabbros (Khedr and Arai, 2016b). **b**) Primitive mantle (PM)-normalized trace-element patterns for clinopyroxenes. **c**) Chondrite (CI)-normalized REE patterns of Opx. **d**) Primitive mantle (PM)-normalized trace-element patterns of Opx in the Korab Kansi gabbronorites. Normalized C1 and PM values are from McDonough and Sun (1995).

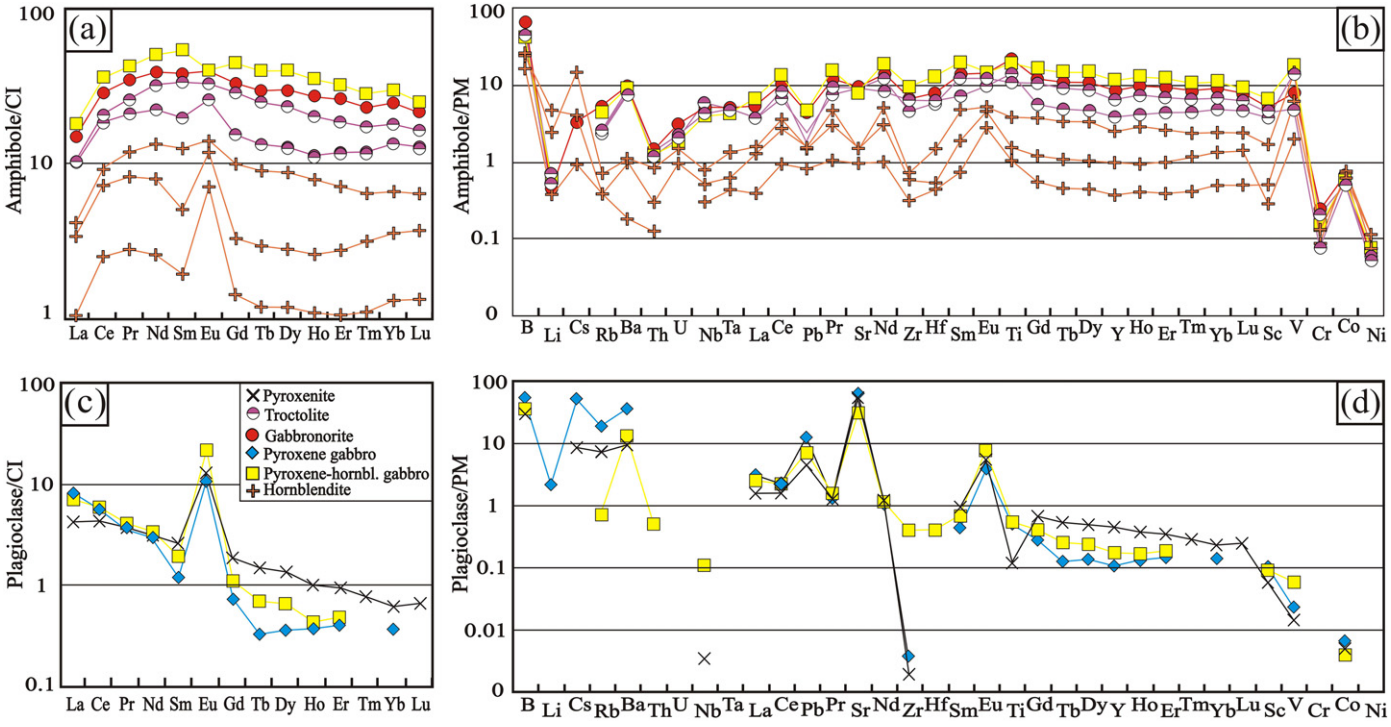

Fig. 6. In-situ trace and rare earth elements of Korab Kansi amphiboles and plagioclase. **a**) Chondrite (CI)-normalized REE patterns of amphiboles. **b**) Primitive mantle (PM)-normalized trace-element patterns of our amphiboles. **c**) Chondrite (CI)-normalized REE patterns of the plagioclase. **d**) Primitive mantle (PM)-normalized trace-element patterns of the plagioclases. Normalized C1 and PM values are from McDonough and Sun (1995).

mixed with 1 ml HNO_3 and 2 ml HF in a capped Savilex teflon beaker, which was left on a hotplate at ~160 °C over two days. To ensure the samples were dissolved completely, 2 × 1 ml concentrated HNO_3 and 1 × 1 ml concentrated HCl were added subsequently to the open beakers until complete evaporation. The dried samples were then diluted with 2 ml 7.5M HNO_3. An aliquot of about 330 μl of the sample was taken for measurement using an Agilent 7700 quadrupole inductively mass spectrometer (ICP-MS) at the Institute of Chemistry - Analytical Chemistry, University of Graz, Austria. The international reference material BHVO-2 and JR-2 were used as standards whereas GS-N, JB-1b, and OPY-1 were measured as external standards to ensure analytical accuracy and quality control. The elements Ge, In and Re were used for the internal drift correction.

The Korab Kansi mafic-ultramafic rocks are fresh as they have low to moderate loss on ignition (LOI) values (0.09–3.66 wt%; Table 3). Their Mg#s [=Mg/(Mg + Fe)] range from 0.42 to 0.73 (Table 3). These rocks show large variations in their major oxides (Table 3). Fine-grained olivine gabbros have the highest Mg# (0.73), MgO (19.29 wt %), Cr (940 ppm) and Ni (621 ppm) contents, and have elevated FeO* contents (12.4 wt. %) but are poor in SiO_2 content (42.44 wt%) relative to other gabbroic rocks (Table 3). They are similar in composition to primary ferropicritic melts (Gibson et al., 2000) and may approximate the composition of the primary Korab Kansi melt. On the other hand, Fe-Ti oxide-rich gabbros have the lowest Mg# (0.43–0.53), and the highest FeO (16.98–21.36 wt%), TiO_2 (1.75–2.95 wt%) and V (506–830 ppm) contents relative to other types (Table 3).

The investigated mafic-ultramafic rocks contain variable contents of REEs and display different REE patterns (Table 3; Fig. 7a). This is related to different mineral assemblages due to fractional crystallization, modal volume% of silicates and variation in abundances of intercumulus liquids. The lowest REE contents are recorded in the Fe-Ti oxide-rich pyroxene gabbros (ΣREE: 5.3–5.8), while pyroxenites have the highest ΣREE (32.1, Table 3).

Chondrite-normalized REE patterns are generally LREE enriched but are LREE-depleted in pyroxenites, gabbronorites, and fine-grained olivine gabbros with $(La/Lu)_N$ values ranging from 0.53 to 9.21 (Fig. 7a). Fe-Ti oxide-rich gabbros show elevated LREE/HREE ratios [e.g., $(La/Lu)_N$ = 5.8–9.2] compared with Fe-Ti oxide-poor gabbros (Table 3). A positive Eu anomaly is present in all samples, weakest in pyroxenites and fine-grained olivine gabbros and strongest in troctolites, olivine gabbros, gabbronorites and pyroxene gabbros, reflecting the role of plagioclase accumulation (Fig. 7a). REE patterns of Korab Kansi gabbroic rocks are broadly similar to layered gabbroic intrusions (Fig. 7a) from Niumaoquan, NW China (Yu et al., 2018), middle Mamakan, Iran (Fazlnia and Alizade, 2013) and Stillwater, USA (Haskin and Salpas, 1992).

Primitive mantle-normalized trace element patterns are enriched in large ion lithophile elements (LILE: Li, Ba, Pb, Sr, La and Eu) + Ti relative to high field strength elements (HFSE: Nb, Ta, Zr, Th, U; Fig. 7b). The V (506–830 ppm) and TiO_2 (1.75–2.95 wt %) contents are high in Fe-Ti oxide-rich gabbroic samples (Table 3) compared with island-arc tholeiitic basalt (V = 242 ppm; TiO_2 = 0.63 wt%, Piercey et al., 2004), reflecting the abundance of ilmenite and titanomagnetite in these samples. Korab Kansi Fe-Ti-bearing gabbros show similarities with the Niumaoquan layered gabbro intrusion containing up to 810 ppm V and 3.45 wt% TiO_2 (Yu et al., 2018).

6. Discussion

6.1. Geothermometry and geobarometry

The crystallization conditions (pressure and temperature) of the Korab Kansi intrusion can be determined through the compositions of pyroxene, hornblende and plagioclase. The pyroxene thermometer (Lindsely Stromer Jr., 1983; Fig. 4c) and amphibole-plagioclase coexisting pairs (Perchuk, 1970; Ulrych et al., 1976; Fig. 8a) give a range of crystallization temperatures ranging from ~700 to 1100 °C, which may reflect a long crystallization time that caused variations in magma compositions during fractional crystallization and cooling. Coexisting amphibole-plagioclase pairs (Fig. 8a) indicate that the

Table 3
Whole-rock major (wt%) and trace elements (ppm) of the Korab Kansi intrusion.

Rock name	Pyroxenite	Troctolite	Olv-gbs	F-olv gbs	Gbs.norite	Fe-Ti rich pyx gbs		Fresh pyx gbs		Alterd pyx gbs	
Sample nam	Sn.9	Kn.41	Kn.9	Sn.16	Sn.4	Kn.2	Kn.15	Kn.43	Sn.2	Kn.4	Sn.5
SiO_2	46.10	46.87	48.24	42.44	50.93	36.98	40.43	49.33	52.69	45.12	48.55
TiO_2	0.88	0.24	1.02	0.87	0.70	2.95	1.75	0.68	0.22	1.06	0.85
Al_2O_3	15.04	18.24	17.20	11.66	11.10	15.98	16.61	16.21	18.94	20.16	21.70
FeO*	10.14	11.06	10.35	12.41	13.31	21.36	16.98	8.50	7.31	11.01	7.47
MnO	0.16	0.14	0.17	0.17	0.23	0.20	0.16	0.13	0.14	0.10	0.09
MgO	6.41	11.74	8.84	19.29	15.02	9.00	10.57	8.77	6.22	7.49	5.46
CaO	19.20	7.88	10.12	7.15	5.64	8.83	6.08	11.00	10.29	8.00	9.09
Na_2O	0.33	2.67	2.71	1.36	1.52	2.16	2.49	2.67	2.89	3.33	3.70
K_2O	0.48	0.13	0.14	0.13	0.13	0.16	0.12	0.15	0.13	0.24	0.31
P_2O_5	0.08	0.02	0.02	0.04	0.02	0.03	0.02	0.03	0.02	0.03	0.02
LOI	0.73	0.09	0.40	3.60	0.78	1.40	3.66	1.54	0.49	2.54	1.79
Total	99.55	99.08	99.21	99.12	99.38	99.04	98.87	99.01	99.34	99.08	99.03
Mg#	0.53	0.65	0.60	0.73	0.67	0.43	0.53	0.65	0.60	0.55	0.57
Cr_2O_3	0.015	0.003	0.011	0.137	0.055	0.016	0.042	0.017	0.001	0.047	0.003
Cr#	0.0007	0.0001	0.0004	0.0078	0.0033	0.0007	0.0017	0.0007	0.0000	0.0016	0.0001
Trace elements (ppm)											
As	<0.5	<0.5	<0.5	<0.5	<0.5	<0.5	<0.5	<0.5	<0.5	<0.5	<0.5
B	2.68	1.54	2.21	3.54	2.86	2.62	3.44	2.58	2.36	2.57	56.50
Ba	188.29	33.49	42.00	33.13	25.00	20.41	35.30	39.96	81.80	66.97	63.62
Be	0.33	0.21	0.23	0.15	0.14	0.22	0.14	0.22	0.45	0.21	0.24
Cd	0.29	0.02	0.05	0.11	0.08	0.08	0.05	0.06	0.11	0.02	0.10
Co	47.40	92.18	85.00	87.66	73.55	110.69	91.47	58.57	32.09	74.66	42.78
Cr	99.60	<20	74.00	939.90	377.70	107.40	287.80	113.50	65.10	322.10	<20
Cs	0.35	<0.1	<0.1	0.35	0.46	<0.1	0.31	0.21	<0.1	0.51	0.86
Cu	1.74	13.60	17.00	38.20	61.44	5.55	20.44	23.81	9.67	10.00	38.27
Ga	18.15	13.26	14.00	9.27	10.30	18.57	17.15	14.82	19.06	20.12	16.76
Hf	1.54	<0.01	0.31	0.71	0.30	0.21	0.13	0.72	0.28	0.18	0.30
Mo	0.15	0.05	0.06	0.14	0.08	0.07	0.07	0.10	0.19	0.07	0.08
Nb	0.20	0.24	0.30	0.84	0.29	0.52	0.36	0.53	0.35	0.41	0.38
Ni	36.70	117.90	95.00	620.60	107.00	113.50	101.00	39.70	<20	90.50	70.20
Pb	0.94	0.32	0.48	0.31	0.32	0.34	0.46	0.50	1.03	0.95	1.39
Rb	7.86	0.25	0.32	0.84	1.55	0.33	0.75	1.11	0.58	3.82	5.44
Sb	<0.1	<0.1	<0.1	<0.1	0.01	<0.1	<0.1	<0.1	0.05	<0.1	0.11
Sc	35.80	3.27	3.36	15.27	16.00	3.93	3.25	25.26	28.37	5.11	7.72
Sn	0.30	0.10	0.18	0.18	0.28	0.38	0.28	0.37	0.12	0.25	0.46
Sr	663.74	487.97	511.00	212.59	266.01	50.86	479.92	373.70	560.61	988.41	596.20
Ta	0.04	0.06	0.06	0.06	0.03	0.07	0.04	0.06	0.05	0.05	0.04
Th	0.07	0.03	0.04	0.05	0.05	0.04	0.05	0.09	0.10	0.06	0.06
U	0.02	<0.01	0.02	0.01	0.01	0.02	0.01	0.03	0.02	0.01	0.01
V	297.30	22.80	148.00	136.20	149.40	830.20	506.30	160.10	162.80	294.30	111.50
Y	22.27	1.03	2.23	11.19	5.36	0.78	0.77	10.19	9.32	1.90	3.06
Zn	69.70	69.80	72.00	85.80	105.64	131.56	110.79	53.66	59.99	74.52	60.53
Zr	52.88	3.31	7.35	20.40	9.38	7.23	4.65	20.49	6.65	5.53	8.99
Li	7.37	2.07	3.45	14.71	0.77	3.79	3.62	6.88	4.82	11.63	4.33
La	1.65	1.07	1.10	1.21	0.82	1.00	0.93	1.98	3.14	1.51	1.12
Ce	5.66	2.17	2.47	3.85	2.11	2.22	2.03	4.81	6.06	3.00	2.86
Pr	1.09	0.27	0.31	0.70	0.32	0.24	0.24	0.79	0.97	0.41	0.37
Nd	6.21	1.12	1.37	4.15	1.70	1.02	0.96	4.32	4.65	1.84	1.86
Sm	2.29	0.24	0.32	1.53	0.55	0.19	0.20	1.44	1.33	0.38	0.52
Eu	1.02	0.46	0.48	0.78	0.38	0.53	0.36	0.78	1.87	0.49	0.53
Gd	3.13	0.23	0.51	1.93	0.74	0.20	0.19	1.89	1.59	0.38	0.60
Tb	0.61	0.03	0.07	0.36	0.14	0.03	0.02	0.33	0.28	0.06	0.10
Dy	4.04	0.20	0.46	2.26	0.99	0.15	0.14	2.07	1.84	0.35	0.61
Ho	0.84	0.04	0.08	0.45	0.21	0.03	0.02	0.41	0.37	0.06	0.12
Er	2.50	0.11	0.23	1.26	0.70	0.09	0.08	1.19	1.05	0.21	0.34
Tm	0.40	0.02	0.03	0.18	0.12	0.01	0.01	0.18	0.16	0.03	0.05
Yb	2.37	0.12	0.19	1.02	0.77	0.08	0.08	0.99	0.99	0.21	0.29
Lu	0.33	0.02	0.03	0.14	0.11	0.01	0.01	0.13	0.14	0.03	0.04
ΣREE	32.13	6.08	7.65	19.81	9.67	5.80	5.30	21.30	24.41	8.96	9.40
(La/Lu)N	0.53	6.67	3.81	0.92	0.75	8.00	9.21	1.60	2.40	5.80	2.83
(La/Sm)N	0.45	2.83	2.15	0.50	0.92	3.25	2.85	0.86	1.48	2.50	1.34
(Nb/La)N	0.12	0.22	0.27	0.69	0.35	0.52	0.38	0.26	0.11	0.27	0.33
Nb/Ta	4.63	4.04	5.00	14.10	9.03	7.65	9.92	9.12	7.58	9.11	9.24
Zr/Hf	34.27	0.00	23.71	28.72	31.44	34.60	35.83	28.49	23.91	31.20	30.26
La/Nb	8.28	4.44	3.67	1.44	2.78	1.91	2.59	3.73	8.94	3.64	2.98
Sm/Zr	0.04	0.07	0.04	0.07	0.06	0.03	0.04	0.07	0.20	0.07	0.06
Th/Ce	0.01	0.01	0.02	0.01	0.02	0.02	0.02	0.02	0.02	0.02	0.02
Th/La	0.04	0.03	0.04	0.04	0.06	0.04	0.05	0.05	0.03	0.04	0.05
Th/Nb	0.34	0.13	0.13	0.06	0.16	0.08	0.13	0.17	0.29	0.16	0.15
Y/Nb	111.97	4.27	7.43	13.26	18.26	1.49	2.13	19.20	26.53	4.58	8.15
Nb/Zr	0.00	0.07	0.04	0.04	0.03	0.07	0.08	0.03	0.05	0.07	0.04
La/Zr	0.03	0.32	0.15	0.06	0.09	0.14	0.20	0.10	0.47	0.27	0.12

Olv gbs: olivine gabbros; F- olv-gbs: fine olivine gabbros; Fe-Ti oxide rich pyx gbs: Fe-Ti oxide rich pyroxene gabbros; Fresh pyx gb: fresh pyroxene gabbros. Alterd pyx gbs: altered pyroxene gabbros

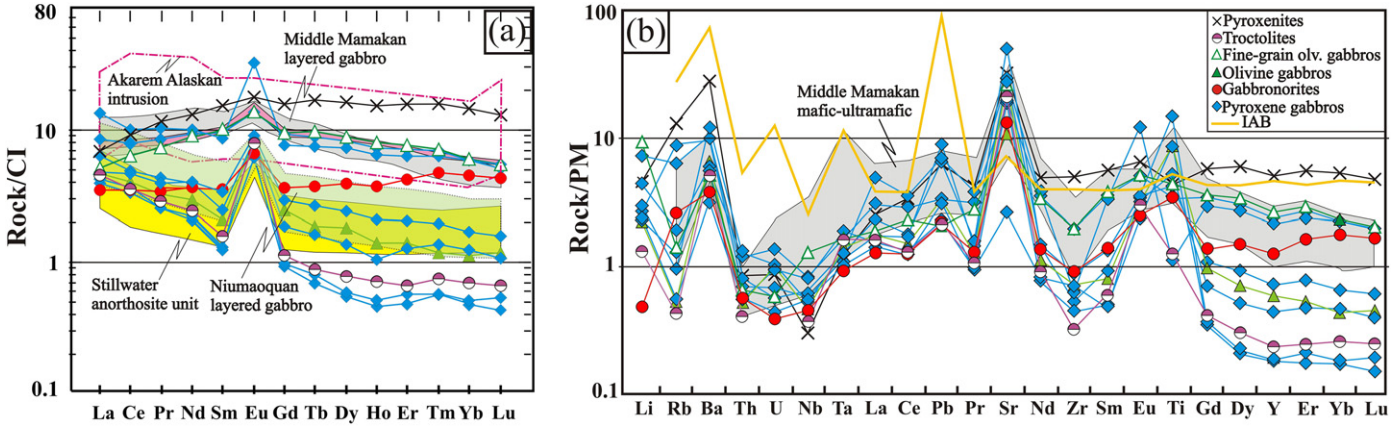

Fig. 7. Whole-rock chemistry of Korab Kansi mafic-ultramafic rocks. **a**) Whole-rock chondrite-normalized REE patterns compared with those from Niumaoquan layered gabbros (Yu et al., 2018), middle Mamakan layered gabbros (Fazlnia and Alizade, 2013), Stillwater mafic-ultramafic intrusions (Haskin and Salpas, 1992), and Akarem Alaskan-type intrusion (Helmy and El Mahallawi, 2003). **b**) Whole-rock primitive mantle-normalized trace element patterns of Korab Kansi mafic-ultramafic rocks compared with island arc basalts (Piercey et al., 2004) and mafic-ultramafic rocks from middle Mamakan intrusion (Fazlnia and Alizade, 2013). Normalized C1 and PM values are from McDonough and Sun (1995).

crystallization sequence started with amphibole peridotites (hornblende dunites) at >1000 °C and ended with pyroxene-hornblende gabbros at ~ 700 °C.

Six coexisting pairs of Opx and Cpx from olivine gabbros (2 pairs) and gabbronorites (4 pairs) reveal temperatures ranging from 853 to 890 °C for gabbronorites and from 924 to 975 °C for olivine gabbros using Wells (1977) and Wood and Banno (1973) thermometry equations. These ranges are consistent with the calculated equilibrium temperature based on thermometry of the Opx-Cpx pairs after Brey and Kohler (1990) yielding 820–830 °C and 917–997 °C for gabbronorites and olivine gabbros, respectively. This is in agreement with T estimated from co-existing amphibole-plagioclase pairs (Perchuk, 1970; Ulrych et al., 1976; Fig. 8a). Coexistence of high temperature amphiboles (e.g. pargasite, tschermakite and edenite) and pyroxenes reflects a temperature range from 900 °C to 1050 °C (Bunch and Okrusch, 1973; Frost, 2006). The Ti and Al^{iv} contents of the primary amphiboles increase strongly with increasing crystallization temperature, and can be used to calculate this temperature (Helz, 1973; Blundy and Holland, 1990). The application of Helz's equation [T (°C) = 273 * Ti + 877] gave temperatures ranging from ~ 881 to 1047 °C for the pargasite crystallization.

Contents of Al, Ti and Na in amphiboles are very sensitive to pressure (Brown, 1977; Hynes, 1982). By using Al_{iv} versus $Na_{(b)}$ of Brown (1977), the analyzed amphiboles estimated 3 to 5 Kbar for primary amphiboles (Fig. 9c). Moreover, the $Al^{(IV)}/Al^{(VI)}$ ratio > 2 for the Korab Kansi primary amphiboles (Supplementary 2) suggests pressure lower than 5 kbar as proposed by Fleet and Barnett (1978). We conclude that the Korab Kansi mafic-ultramafic rocks crystallized at pressure mostly lower than 5 Kbar and temperature ranging from ~700 to 1100 °C. These pressure estimates reflect crystallization depths from <10 to 15 km, within the upper crust.

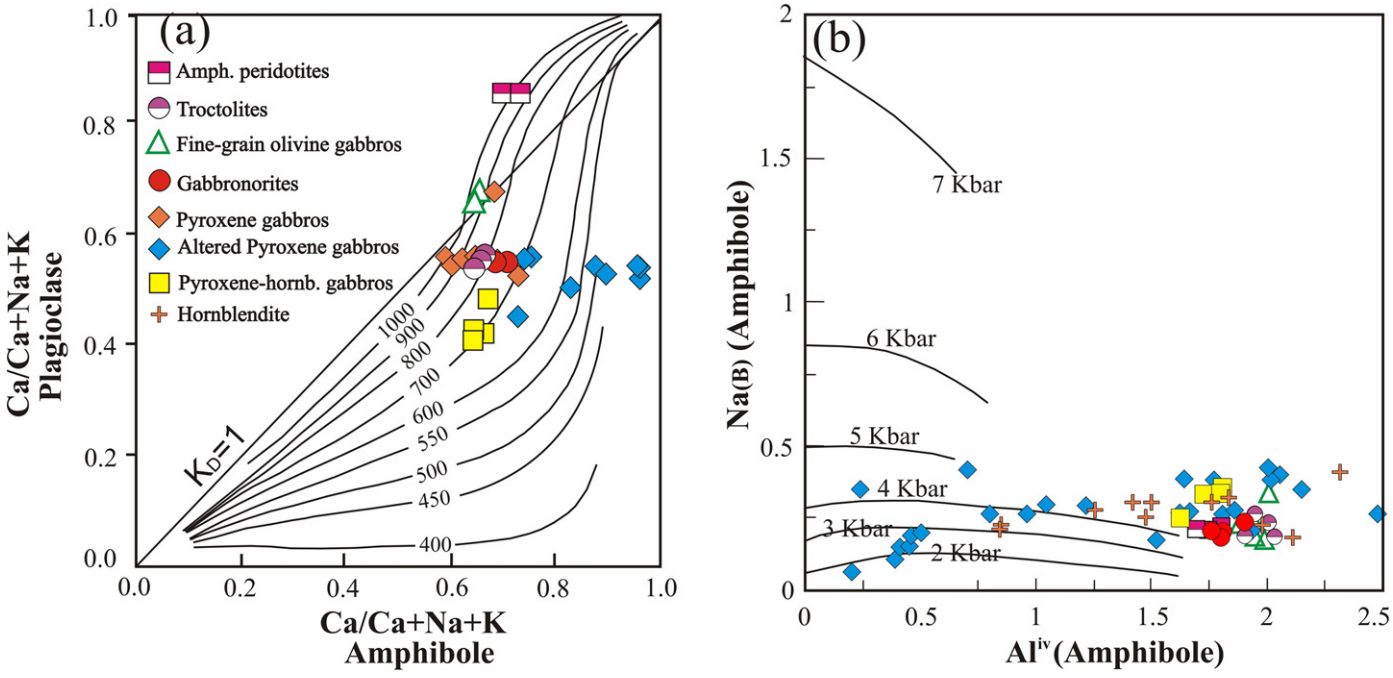

Fig. 8. Thermometry and barometry of the Korab Kansi mafic-ultramafic intrusion based amphiboles and amphibole-plagioclase pairs **a**) Thermometry of amphibole-plagioclase pairs in the distribution diagram (Perchuk, 1970; Ulrych et al., 1976). **b**) Barometry as Al_{iv} vs. $Na_{(B)}$ diagram for the studied amphiboles (Brown, 1977).

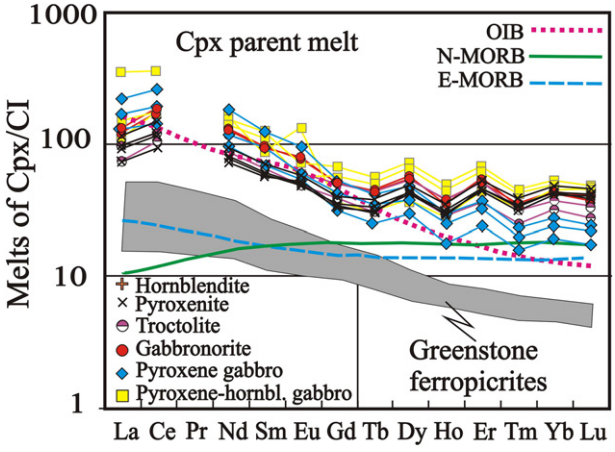

Fig. 9. Cl-normalized REE patterns for calculated melts in equilibrium with Cpx from the Korab Kansi mafic-ultramafic intrusion. Cpx/melt partition coefficients are from Hart and Dunn (1993) and Stosch (1982). Ferropicrites in greenstone belts are after Thurston (2015). Ocean island basalt (OIB), normal mid-ocean ridge basalt (N-MORB) and enriched mid-ocean ridge basalt (E-MORB) compositions are from Sun and McDonough (1989). Normalized C1 and PM values are from McDonough and Sun (1995).

6.2. Nature and evolution of Korab Kansi parental magmas

Fractional crystallization and magmatic evolution of the Korab Kansi intrusion can be deduced from compositions of olivine, Cpx, amphibole and plagioclase (Supplementary 2; Figs. 4, 10c). For instance, olivine forsterite content (Fo) systematically decreases from amphibole peridotites (Fo = 85.6 on average) to troctolites (Fo = 69.5) and olivine gabbros (Fo = 68.5) (Supplementary 2; Fig. 4a). This is consistent with Cpx compositions, which show a wide range of Mg# (0.57-0.95) and systematically decrease from troctolites (Cpx Mg#, 0.87 on average), olivine gabbros (Cpx Mg#, 0.8), gabbronorites (Cpx Mg#, 0.79), pyroxene gabbros (Cpx Mg#, 0.77) to pyroxene-hornblende gabbros (Cpx Mg#, 0.71) (Supplementary 2; Fig. 10c) due to the fractional crystallization of their parental melts (e.g., Zhou et al., 2005; Bai et al., 2012). Cpx REE contents increase with differentiation, with lower average concentrations (ΣREEs = 37.7 ppm) in pyroxenites and more in pyroxene-hornblende gabbros (ΣREEs = 61.1 ppm; Table 2). In addition, plagioclase compositions decrease from bytownite ($An_{85.7-85.8}$) in peridotites, labradorite ($An_{50.6-68.9}$) in troctolites, olivine gabbros and pyroxene gabbros, and andesine ($An_{40.9-48.4}$) in pyroxene-hornblende gabbros (Fig. 4e; Table 1; Supplementary 2). The systematic decrease of anorthite content (An) in plagioclase reflects a fractional crystallization trend from peridotites to pyroxene-hornblende gabbros (Fig. 4e). Amphiboles also show a systematic decrease of Mg#, 0.97, 0.79, 0.77, 0.69 and 0.64 on average for peridotites, troctolites, pyroxene gabbros, gabbronorites and pyroxene-hornblende gabbros, respectively (Supplementary 2, 4c, d). Similar to Cpx (Table 2), REE concentrations of Korab Kansi amphiboles increase with fractionation from troctolites (ΣREEs = 51 ppm, on average) to pyroxene-hornblende gabbros (ΣREEs = 97.4 ppm) (Table 2). Consequently, the crystallization sequence of the Korab Kansi intrusion is olivine + Fe-Ti oxides + pargasite (dunites), olivine + plagioclase ± Cpx (fine-grained olivine gabbros), olivine + plagioclase (troctolites), coarse olivine + plagioclase + Cpx (coarse olivine gabbros), plagioclase + Cpx (pyroxene gabbros), plagioclase + Cpx + Opx (gabbronorites), and plagioclase + Cpx + hornblende (pyroxene hornblende gabbros) (Table 5; Fig. 14).

Field observations, petrography and whole rock chemistry also reflect the importance of fractional crystallization for evolving Korab Kansi magmas. Evidence of this fractionation can be summarized as follows: 1) the dominant cumulate textures (Fig. 3a); 2) the dominant small-scale rhythmic layers (Fig. 2c); 3) the widely variable Ni (<20–620 ppm) and Cr (<20–939 ppm) contents Table 3); and 4) the large variations of major oxides, i.e., 0.22–2.95 wt% TiO_2, 11.1–21.7 wt % Al_2O_3, 7.31–21.36 wt% FeO, 5.46–19.29 wt% MgO, 5.64–19.2 wt% CaO and 0.33–3.7 wt% Na_2O (Table 3).

The fine-grained olivine gabbro (Mg#, 0.73) from the Korab Kansi intrusion is depleted in HREE (e.g. Lu = <10 × chondrite) (Fig. 7b) and has whole-rock compositions (Table 3) similar to primary ferropicrites (Gibson et al., 2000) and Lalibela ferropicrites in the Ethiopian large igneous province with compositions of FeOt (14.0 wt %), TiO_2 (3.84 wt%), CaO (10.0 wt%), MgO (13.9 wt%), Al_2O_3 (8.6 wt%),

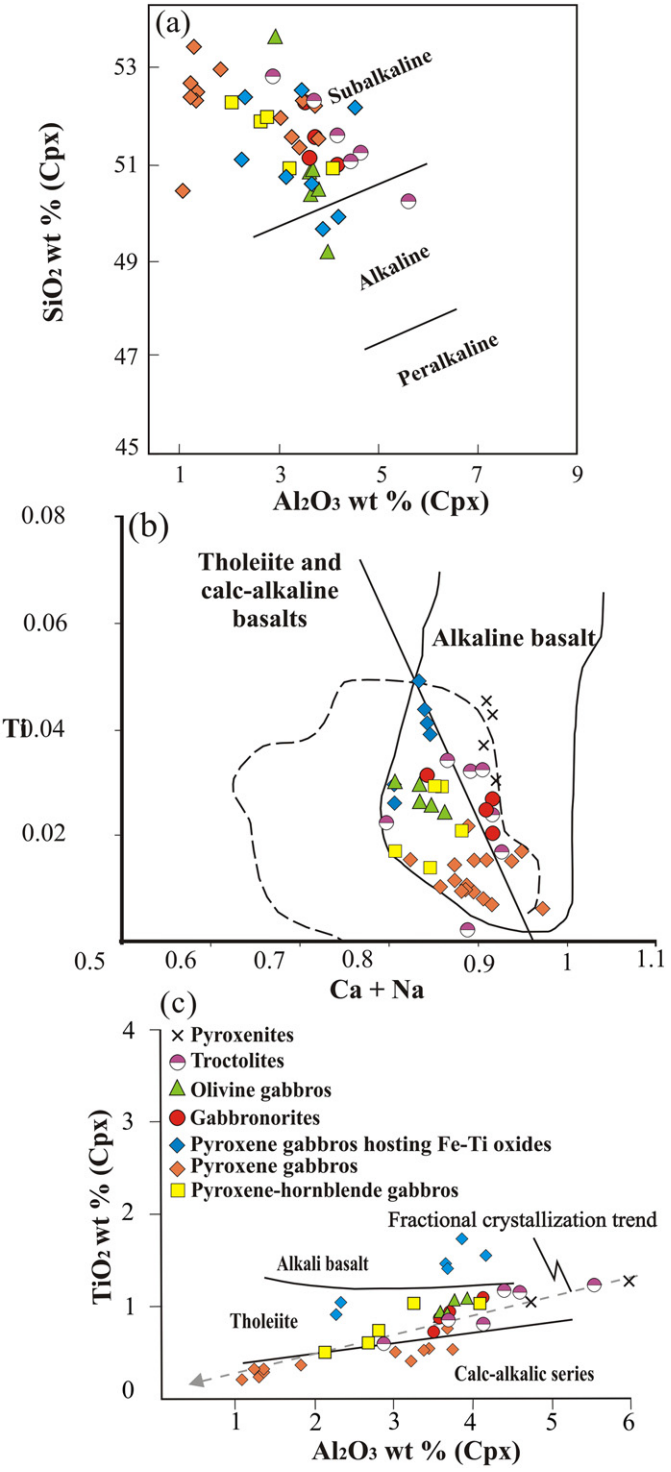

Fig. 10. Chemical compositions of Korab Kansi clinopyroxenes showing type of magmas. **a**) Al_2O_3 vs. SiO_2 diagram of Cpx (Le Bas, 1962). **b**) Cations of Ca + Na versus Ti of Cpx (Leterrier et al., 1982). c) Al_2O_3 against TiO_2 of Cpx (Fiala et al., 1975; Ulrych, 1986).

Na_2O (1.8 wt%), Ni (501 ppm), V (407 ppm) and Cr (195 ppm) (Desta et al., 2014). Mineral chemistry of both ferropicritic olivines (Fo79–88.9) and Cpxs (Mg# = 77–88, TiO_2 = 0.84–1.7 wt%, Al_2O_3 = 1.2–2.7 wt%, depleted Nb, Zr) in Lalibela ferropicrites (Desta et al., 2014) matches Korab Kansi olivine (Fo 78–86) and Cpx chemistry, i.e., Cpx Mg# = 60–84, TiO_2 = 0.6–1.5 wt%, Al_2O_3 = 2.7–6.7 wt% and depleted Nb and Zr (Tables 1; Supplementary 2; Figs. 4c, 5b). Moreover, the abundance of olivines in all rocks and the presence of olivine-rich cumulates such as Fe-Ti oxide-rich dunites and amphibole dunites (Fig. 3a–b) also indicate a ferropicritic parental magma (Erdenesaihan et al., 2014). From these results, the Korab Kansi fine-grained olivine gabbros (Table 3; Fig. 7) are a kind of frozen melt nearly approximating the primary magmas from which the cumulate mafic rocks evolved.

Cpxs from the Korab Kansi intrusion display convex-upward REE patterns, similar to Cpx REE patterns of ferropicrites and picritic ferrobasalts from Lalibela (Desta et al., 2014) and tholeiitic lavas from Kilauea (Norman et al., 2005) (Fig. 5a). Korab Kansi Cpx REE patterns also resemble Cpx REE patterns of Motaghairat layered mafic-ultramafic intrusion, interpreted to have been derived from fractional crystallization of subduction-related high-Mg tholeiitic parental melts (Abdel Halim et al., 2016). The composition of Korab Kansi Cpxs also indicates a subalkaline, tholeiitic affinity of their parental melts (Fig. 10). The Korab Kansi mafic-ultramafic intrusion was possibly derived from Fe-Ti-rich parental melts such as ferropicritic melts of tholeiitic affinity. This can also be concluded from the abundance of olivines as cumulate dunites and olivine gabbros, the enrichment of Fe-Ti oxides as intercumulus disseminated grains in most of the investigated rocks (Fig. 3a, d, f, h), the occurrence of Fe-Ti oxide rich layers (Fig. 2a, b, h) and the presence of exsolution lamellae of ilmenite in Cpx (Fig. 3j). The ferropicritic melts, which are more enriched in Fe, Ti and V relative to tholeiitic melts, can explain the Fe-Ti-V ore deposits (Fig. 2a, b, h) in the Korab Kansi intrusion.

The composition of melts in equilibrium with Cpxs in the Korab Kansi gabbroic rocks (Fig. 9) were calculated using the Cpx/melt partition coefficients (Hart and Dunn, 1993; Johnson, 1998). Their chondrite-normalized REE patterns (McDonough and Sun, 1995) exhibit a concave downward shape with enrichment in MREE, like ferropicrites crystallized from olivine-rich mantle melts of Archean greenstone belts (Thurston, 2015) and ocean island tholeiitic basaltic melts (Sun and McDonough, 1989) (Fig. 9). This is evidence that the Korab Kansi Cpxs crystallized from ferropicrite-like melts of tholeiitic affinity.

Based on the whole-rock chemistry, Korab Kansi gabbroic rocks have a tholeiitic affinity with minor calc-alkaline tendency (Fig. 13a). This is confirmed by REE patterns of the gabbroic rocks (Fig. 7a) that are like those of the Mamakan layered gabbroic intrusion, which crystallized from tholeiitic basaltic magmas in an island arc setting (Fazlnia and Alizade, 2013). The Korab Kansi intrusion is also similar in REE patterns to Niumaoquan layered gabbros (Yu et al., 2018) and Stillwater mafic-ultramafic intrusions (Haskin and Salpas, 1992), but differs in REE concentrations and patterns with those of the Dahanib Alaskan intrusion (Fig. 7a). The Niumaoquan gabbroic intrusion (North Xinjiang, China) hosts a Fe-Ti oxide deposit and is characterized by enriched LILE, like the Korab Kansi intrusion (Fig. 7a). Its parental magma was produced by interactions between metasomatized lithospheric mantle and depleted asthenospheric melts (Yu et al., 2018). Nd and Sr isotopic evidence ($^{87}Sr/^{86}Sr$ = 0.7024 to 0.7029 and ε-Nd(t) = +4.5 to +7.9) of the Korab Kansi gabbros (Zimmer et al., 1995) indicates a dominance of asthenospheric melt sources. These melts had enriched LREE, Fe and Ti (see Figs. 7a, 9), suggesting a plume-like mantle source. This is consistent with the high Ti, Nb and Ta values in the Korab Kansi primary amphibole (Fig. 6b; Table 2), suggesting volatiles-rich ferropicrite parental melts that could be derived either from metasomatized mantle or a volatile-bearing mantle plume (Fiorentini et al., 2008). Melts enriched in Fe-Ti oxides (See Fig. 3) are found in some large igneous provinces by formation of tholeiitic ferropicrites with high FeO* (>12 wt%) and MgO (>19 wt%) (Gibson et al., 2000; Erdenesaihan et al., 2014; Desta et al., 2014), like the fine-grained olivine gabbro (Sn-16; Table 3) in the Korab Kansi intrusion. This suggests interactions between metasomatized lithospheric mantle and upwelling asthenospheric melts or a mantle diaper to produce mixed melts that formed the Korab Kansi layered intrusion.

The hydrous nature of parental ferropicritic magmas of the Korab Kansi intrusion can be deduced from petrography (Fig. 3) and chemistry (Figs. 7–11) as follows: 1) Abundance of amphiboles in all rock varieties from peridotites to pyroxene-hornblende gabbros (Fig. 3b, e, i, k). With increasing water content of the magma after crystallization of anhydrous phases, the hornblende oikocrysts started to crystallize in large quantities at the expense of Cpx due to stabilizing calcic amphiboles in the interstitial liquid (Zhang et al., 2009), forming pyroxene-hornblende gabbros (Fig. 3k). For this reason, the amount of amphiboles increases toward the highly fractionated pyroxene-hornblende gabbros (Fig. 3k); 2) The dominance of Ca-rich plagioclase (anorthite and labradorite) in the examined gabbroic rocks (Fig. 3i; Supplementary 1) suggests crystallization from hydrous melt rich in Al and poor in Na (Sisson and Grove, 1993; Claeson and Meurer, 2004); 3) Gabbroic rocks (Fig. 7b) and their minerals (Figs. 5b, d; 6b, d) are enriched in fluid mobile elements (e.g., Li, B, Cs, Ba, Sr, Pb); and 4) The dominance of titanomagnetite over ilmenite (Fig. 3, 4f) is also related to high water contents, which increases oxygen fugacity and the Fe_2O_3/FeO ratio (Yu et al., 2018).

The oxygen fugacity (fO_2) of Korab Kansi olivine gabbros and troctolites was calculated based on the fayalite-magnetite-quartz (FMQ) buffer (Ballhaus et al., 1990, 1991). It gives a very narrow range from FMQ +4.1 to FMQ +4.3 (Fig. 11). These fO_2 high values reflect highly oxidation conditions during formation of the Korab Kansi intrusion, forming thick titanomagnetite-ilmenite deposits (Fig. 2a, b, h). They are compared with those of MORB, arc basalt, island-arc basalt and ocean-island basalt (Ballhaus et al., 1990, 1991), where the Korab Kansi rocks are close to the fO_2 field of island-arc basalt and far away from that of MORB (Fig. 11). This is evidence of an island-arc setting for the Korab Kansi intrusion, where magma was oxidized due to subduction-related fluids or recycling of crustal hydrophilic components into the upper mantle (Ballhaus et al., 1990). High fO_2 was also recorded in the layered mafic–ultramafic intrusion in the Wajilitag large igneous province in NW China, which is similar in chemical composition, showing OIB-like compositional affinity (Fig. 9), and highly

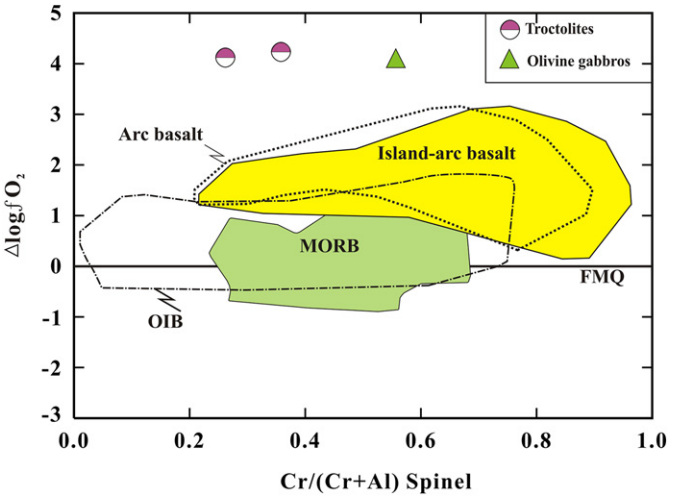

Fig. 11. Oxygen fugacity (fO_2) versus spinel Cr# of Korab Kansi olivine gabbros and troctolites based on fayalite-magnetite-quartz (FMQ) buffer (Ballhaus et al., 1990, 1991). The fO_2 fields of MORB (depleted and enriched MORB), arc basalt (from Alaskan-type intrusion and cumulate inclusions), island-arc basalt and their cumulate nodules and OIB (ocean-island basalt and their mantle xenoliths) (Ballhaus et al., 1990, 1991) are used for comparison.

including Fe–Ti oxide mineralization (Cao et al., 2014) to the Korab Kansi intrusion. Both Korab Kansi and Wajilitag intrusion (Cao et al., 2014) accumulated significant Fe–Ti oxides during magmatic differentiation under high fO_2 and volatile-rich conditions.

Evidence supporting the high oxygen fugacity (fO_2) of Korab Kansi parental magmas are summarized as follows: 1) The ultramafic-mafic rocks contain considerable amounts of titanomagnetite, magnetite and ilmenite as intercumulus phases (Fig. 3d, f, h) or as massive ore layers (Fig. 2a, b, h), suggesting crystallization from Ti-rich ferropicritic melts under strongly oxidizing conditions (e.g., Juster et al., 1989; Toplis and Carroll, 1995); 2) The crystallization of more titanomagnetite than ilmenite in Korab Kansi mafic-ultramafic rocks (Fig. 3d, f, h) was largely controlled by high fO_2 and temperature (e.g., Hill and Roeder, 1974; Zimmer et al., 2010); 3) Fe-Ti oxides are rich in V_2O_5 (up to 4.3 wt%; Supplementary 3), reflecting strongly oxidizing conditions (e.g., Toplis and Corgne, 2002); 4) Preferential incorporation of V in ilmenite (V_2O_5, 3.6–4.3 wt%) relative to magnetite (V_2O_5, 1.4–1.8 wt%; Supplementary 3) has been attributed to higher oxygen fugacity of parental melts (e.g., Schulling and Feenstra, 1980); 5) The presence of $FeTiO_3$-$MnTiO_3$ (MnO up to 3.7 wt%; Supplementary 3) solid solution in ilmenite reflects crystallization at high oxygen fugacity (e.g., Deer et al., 1992); 6) The dominance of trellis intergowth of ilmenite in titanomagnetite (Fig. 3d) is due to oxidizing condition during its formation (Tan et al., 2016). The high fO_2 coupled with high water content is a characteristic feature of island arc magmas (Khedr and Arai, 2010; Plank et al., 2013; Khedr and Arai, 2016b). High fO_2 is vital for formation of the Korab Kansi mafic-ultramafic intrusion, where it is one of the most important factors for controlling precipitation of Fe-Ti oxides, along with temperature and H_2O content (Kress and Carmichael, 1991).

Finally, the Korab Kansi layered mafic-ultramafic rocks were possibly intruded through multiple pulses of magmas at different stages of the island arc evolution, starting with the injection of more primitive magmas to form rocks of group 1 (e.g. peridotites, pyroxenites, fine-grained olivine gabbros, troctolites) at the subduction initiation stage (incipient-arc stage) and ended with the evolved rocks of group 2 (e.g. pyroxene gabbros, gabbronorite, pyroxene hornblende gabbros) in compressional setting during submature/mature arc stages. The Korab Kansi mafic-ultramafic rocks were crystallized from mantle-derived hydrous ferropicritic melts of tholeiitic affinity that has evolved by silicate fractionation under high fO_2 in the presence of subduction-related fluids to form calc-alkaline magmas during maturation of an island arc system.

6.3. Petrogenesis and geodynamic evolution of the Korab Kansi intrusion

The study of Neoproterozoic mafic–ultramafic intrusions in the SED of Egypt, like the Korab Kansi intrusion, is a key to understand the geodynamic evolution of the Arabian Nubian Shield (ANS). The Korab Kansi complex is considered to be a syn-tectonic layered mafic-ultramafic intrusion (Fig. 2a–c), showing characterestics that distinguish it from ophiolitic mafic-ultramafic rocks and Alaskan-type complexes. It is characterized by: 1) a lack of metamorphic overprint and minor serpentinization, 2) a layered structure (Fig. 2c) and cumulate texture (Fig. 3a) as evidence of fractional crystallization, 3) having intrusive contact with the surrounding rocks (e.g. ophiolites and volcanic schist) and absence of thrust or tectonic contacts (Fig. 1), 4) the absence of the Moho transition zone or any sign of intact or dismemberd ophiolitic sections, 5) the absence of concentric zonation, 6) having low Fo content for olivine (Fo: 67.9–85.7) when compared with olivine (Fig. 4a) from Egyptian ophiolites (Fo > 88; Khedr and Arai, 2013, 2016a, 2017) but are very similar to olivine Fo of both Egyptian layered mafic-ultramafic rocks (Fo: 70.6–85.9; Abdel Halim et al., 2016) and the Xinjie layered intrusion of SW China that hosts significant Fe-Ti oxide deposits (Fo: 72–76; Dong et al., 2013), 7) having two generations of amphiboles such as pargasite with high Al, Na and Ti contents indicating magmatic origin and crystallization from mantle-derived melts (Supplementary 4, c, d), whereas actinolite of the hydrothermal origin (Girardeau and Memel, 1982) was formed during cooling after magmatic formation (Supplementary 4, c, d), and 8) having very low concentrations of Cr_2O_3 (0.03 wt% on average; Table 3) in the gabbroic rocks and their pyroxenes, amphiboles and opaque minerals (Cr_2O_3 < 0.1 wt%; Supplementary 2, 3). The Cr and Ni content is very low in the Korab Kansi ultramafic rocks (Cr< 100 ppm) and mafic rocks (Cr, 20–380 ppm; Table 3), except for the fine-grained olivine gabbros (Cr = 940 ppm; Ni = 621 ppm). The peculiar chromite-free dunites and pyroxenites (Table 3) have low magnesium olivine (Fo_{86-68}) and low Cr and Ni contents, suggesting fractionation of Mg-rich olivine and chromite in some deeper part (upper mantle) possibly to form the chromite-dunite complex. The Korab Kansi area is the extension of the Gerf ophiolite that includes chromite-dunite associations (GSE, 2002). We expect that the primitive magmas for the Korab Kansi complex form Cr-free cumulate dunites (rich with ilmenites), pyroxenites, olivine gabbros and other gabbroic rocks, after formation of the chromite-dunite complex.

The current study excludes the Alaskan-type origin of the Korab Kansi intrusion based on, geology (Figs. 1, 2; Supplementary 1), lithology (Fig. 3; Table 4) and chemistry (Figs. 4a, 5a, 7 and 12c). There is no concentric zonation from ultramafic rocks in the core to gabbroic rocks at the rim, in contrast to what is expected for Alaskan-type complexes found elsewhere in the SED of Egypt (Farahat and Helmy, 2006; Helmy et al., 2008; Khedr and Arai, 2016b). The occurrence of ultramafic rocks at the base of the Korab Kansi intrusion or at the contact with ophiolitic rocks (Fig. 1b; Supplemenatry 1), forming several layers (Fig. 2), is a line of evidence for the layered origin not the Alaskan origin. In addition, layered mafic-ultramafic complexes in Egypt consist mainly of mafic rocks (mainly pyroxene gabbros > ~70 vol%) with subordinate ultramafic rocks (<10 modal volume %) (Abu El Ela, 1991; Abu Anbar, 2001; Abdel Halim et al., 2016), similar to the Korab Kansi mafic (mainly pyroxene gabbros; Fig. 1b; Supplementary 1) to ultramafic rocks of volume ratio ~95: 5% (Table 4). Alaskan mafic rocks in Egypt are mainly hornblende gabbros to gabbronorites, in contrast to pyroxene gabbros and olivine gabbros in layered intrusions (Table 4). Also, the layered intrusions (e.g., Abu Ghalaga, Akab El Negum and Abu Fas) in Egypt host Fe-Ti-V ore layers (Nasr et al., 2000; Makhlouf et al., 2008), like the Korab Kansi one (Fig. 2a, b, h), in contrast to Egyptian Alaskan intrusions are characterized by sub-economic Cu–Ni-S-PGE deposits (Helmy and Mogessie, 2001; Helmy, 2004). Mineral and whole rock chemistry of the investigated rocks also support an interpretation that the Korab Kansi intrusion is a layered mafic-ultramafic body (Figs. 5a, 7a, 12c).

Zircons from Korab Kansi layered gabbros were dated at 741 ± 21 Ma based on $^{207}Pb/^{206}Pb$ zircon evaporation technique (Kröner et al., 1992). These layered gabbros also yielded an age of 721 ± 37 Ma obtained from their Sm-Nd whole-rock isochrons (Zimmer, 1989) and 720 ± 9 Ma based on their whole-rock $^{147}Sm/^{144}Nd$ versus $^{143}Nd/^{144}Nd$ data (Zimmer et al., 1995). So, we adopt 741 ± 21 Ma as the main average age of the Korab Kansi intrusion. This age is consistent with island-arc stages of the ANS (Stern et al., 1989) and is similar to ages of island-arc volcanics (720–770 Ma after Stern and Hedge, 1985), Shadli rift-related metavolcanics (~712 Ma, Stern et al., 1991) and some Alaskan-type rocks (Sm/Nd model age of 770 ± 20 Ma, Farahat and Helmy, 2006) in the SED of Egypt. From these results, the formation of the Korab Kansi layered intrusion was possibly contemporaneous with Abu Hamamid (770 Ma) but younger than Genina Gharbia Alaskan-type intrusions (963±81Ma; Helmy et al., 2014) (Table 4). It is genetically related to the formation of island-arc metavolcanic rocks and some Alaskan-type intrusions. Both Alaskan and layered intrusions are considered as roots or feeder conduits of island-arc volcanoes. We think that the Korab Kansi Fe-Ti-bearing intrusion is the oldest layered intrusion in Egypt (see Table 4) relative to the other (age < 700 Ma) free of Fe-Ti deposits. Its formation possibly represents a transitional stage between Alaskan intrusion and younger layered intrusions (free of Fe-Ti ores) in the Nubian Shield. We suggest that Cryogenian-

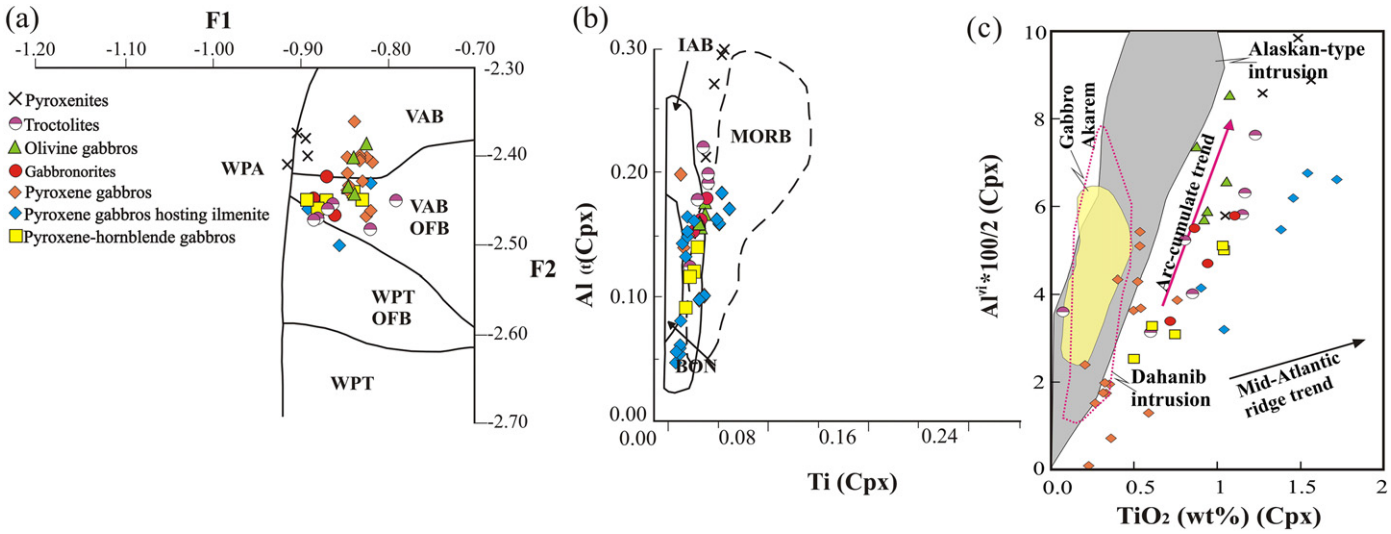

Fig. 12. Mineral chemistry of Korab Kansi clinopyroxenes showing the tectonic setting of their host rocks. **a**) F1 vs. F2 diagram of Cpx (Nisbet and Pearce, 1977). **b**) Cations of Ti versus $Al^{(t)}$ of Cpx (Beccaluva et al., 1989). **c**) TiO_2 against $Al^{iv}100/2$ of Cpx (Loucks, 1990). The fields of Alaskan-type intrusions (Himmelberg and Loney, 1995), and Alaskan-type complexes in Egypt such as Gabbro Akarem complex (Helmy and El Mahallawi, 2003) and Dahanib intrusion (Khedr and Arai, 2016b) are used for comparison.

Tonian mafic intrusions in SE Egypt can be subdivided into Alaska-type intrusions that are enriched in PGEs whereas Korab Kansi-type layered intrusions are enriched in Fe-Ti-V deposits.

Chemistry of Cpxs is useful for inferring tectonic setting of the intrusion (Fig. 12). Korab Kansi Cpxs plot in the volcanic arc or island-arc basalt fields, and follow the arc cumulate trend (Fig. 12a–c). They and their host gabbros can be assigned to an orogenic setting (e.g., island arc) (e.g. Nisbet and Pearce, 1977; Beccaluva et al., 1989; Loucks, 1990). The Korab Kansi intrusion is considered to have an arc-related origin. The depleted LREEs relative to HREEs of the Cpxs (Fig. 5a) [$(La/Lu)_N$ = 0.2–0.9] may be attributed to high degress of partial melting of the mantle source under the influence of slab-derived fluids as expected above a subduction zone in an island arc setting. The Cpxs have less HFSE (especialy Nb and Ta; 0.04-0.9 time PM; Fig. 5b), but have more fluid mobile elements or LILEs (e.g., B, Li, Cs, Rb, Ba; Fig. 5b) that may reflect the addition of these elements from the subducted slab (Ryan et al., 1995; Khedr et al., 2010; Khedr and Arai, 2016b). Enrichment of LILEs and depletion of HFSE in Cpxs (Fig. 5b) reflect island-arc signatures of the studied intrusion (Bédard et al., 2009; Khedr et al., 2010; Khedr and Arai, 2016b). In addition, the Neoproterozoic mantle was depleted in Nb and Ta (Khedr and Arai, 2016b), where slab-derived fluids that are rich in LILEs can explain the depleted HFSEs and enriched LILEs of the Korab Kansi parental magma. The chondrite-normalized REE patterns of the Korab Kansi Cpxs resemble those of the Motaghairat mafic-ultramafic complex in the SED of Egypt (Abdel Halim et al., 2016; Fig. 5a) because both are layered intrusions generated in a subduction zone (Abdel Halim et al., 2016).

Korab Kansi mafic-ultramafic rocks are highly enriched in LILE (Li, Rb, Ba, Pb and Sr; Fig. 7b) and LREE relative to HFSE (e.g. Th, U, Nb, Ta and Zr) and HREE (Fig. 7), respectively. This is consistent with the characteristics of an island-arc setting and also reflects subduction-zone signatures, where LILE and LREE are added from subduction-related hydrous fluids to the mantle source (e.g., Perfit et al., 1980; Khedr et al., 2010, 2014; Wehrmann et al., 2014; Khedr and Arai, 2016b). The HREE and HFSE are immobile and insoluble in subduction-related fluids. Consequently, they can be used as guides for the mantle composition from which the magmas that formed the investigated mafic-ultramafic rocks were derived (Pearce and Parkinson, 1993; Khedr et al., 2010, 2014). The depletion of HFSE in the examined gabbroic rocks (Fig. 7b) suggests that the Korab Kansi intrusion was derived from a depleted mantle source and that HFSE were not added from the slab-derived fluids during mantle metasomatism (Khedr and Arai, 2016b). Moreover, by using Th/Ta versus Ta/Hf diagram (Fig. 13c), most samples fall in and around the depleted mantle source field (DMM) except three Fe-Ti oxide-rich samples that fall near the oceanic island basalt field (OIB). The fine-grained olivine gabbros, which are frozen melts and may represent the first stage of mafic rocks crystallized from tholeiitic ferropicritic melts and plot in the DMM field (Fig. 13c).

The chondrite-whole rock REE normalized patterns of Korab Kansi gabbroic rocks (Fig. 7a) are similar to those of Niumaoquan layered gabbros (Yu et al., 2018) and the Mamakan layered gabbroic intrusion thought to have formed in an intra-oceanic arc (island arc) setting (Fazlnia and Alizade, 2013). In addition, the PM-normalized trace element patterns of the Korab Kansi rocks are similar to those of island arc basalts (Piercey et al., 2004) and Mamakan island-arc layered gabbroic rocks (Fazlnia and Alizade, 2013) (Fig. 7b), which crystallized from tholeiitic basaltic magmas formed from the partial melting of metasomatized spinel peridotites in the mantle wedge (Fazlnia and Alizade, 2013). This similarity of whole rock chemistry with the Mamakan layered gabbroic intrusion (Fig. 7) and the marked negative HFSE (U, Th, Zr, Nd, Nb, Sm and Ta) and positive Ba, Sr and Li anomalies of Korab Kansi rocks (Fig. 7) are features of subduction-related magmas in the island-arc setting (Fazlnia and Alizade, 2013). Moreover, the investigated intrusion is similar in whole-rock REE patterns and enrichment of LILEs and depletion of HFSEs (Fig.7) to the Niumaoquan layered gabbroic intrusion (China) that hosts Fe-Ti oxide deposits (Yu et al., 2018). This Niumaoquan intrusion crystallized from parental magma produced by the interactions between metasomatized lithospheric mantle and asthenospheric melts during the island arc stage. Like the Niumaoquan intrusion, the parental hydrous ferropicritic melts of the Korab Kansi intrusion have tholeiitic affinity, and are possibly resulted from highly partial-melting degrees of metasomatized lithospheric mantle by upwelling asthenospheric melts (see chemistry of Cpx, Figs. 5, 10, 12) in the presence of a strong flux of slab-derived fluids above a subduction zone.

It is well known that tholeiitic to calk-alkaline magmas are dominant in island arc settings. Consequently, the tholeiitic to calk-alkaline characters (Figs. 10, 13a) of the Korab Kansi rocks may reflect a primitive island-arc setting. These rocks are similar in FeO, MgO and $Na_2O + K_2O$ (Fig. 13a) to arc-related mafic cumulate rocks (Beard, 1986), and plot in the island-arc tholeiitic field by using TiO_2-MnO-P_2O_5 (MullenStromer Jr., 1983; Fig. 13b). The high fO_2 coupled with high water contents in the parental melts of Korab Kansi rocks is a characteristic feature of arc magmas (Plank et al., 2013).

Table 4
Comparison between KorabKansi intrusion and other layered intrusions as well as Alaskan-type intrusions

	Korab Kansi intrusion	Layered intrusions in Egypt	Alaskan-type intrusions in Egypt	Worldwide layered intrusions
Intrusion Outcrops	– Korab Kansi intrusion surrounded by ophiolites and intruded by syntectonic granites	– Atud (Ghoneim, 1988; Abu El Ela, 1991); Um Rus (Abu Anbar, 2001); Motaghairat (Abdel Halim et al., 2016); Abu Ghalaga, Akab El Negum and Abu Fas (Nasr et al., 2000; Makhlouf et al., 2008).	– Abu Hamamid (Farahat and Helmy, 2006); Gabbro Akarem (Helmy and El Mahallawi, 2003); Genina Gharbia (Helmy et al., 2014); Dahanib (Khedr and Arai, 2016b)	– Panzhihua Intrusion in China (Zhou et al., 2005); Sept Iles in Canada (Namur et al., 2010); Skaergaard in East Greenland (Jang et al., 2001); Bushveld in South Africa (Von Gruenwaldt, 1994); Koillismaa Fe-Ti-V--bearing intrusion in NE Finland (Karinen, 2010).
Rock Types	– Amphibole peridotites, pyroxenites and bands of hornblendite associated with Fe-Ti cumulate dunites or Fe-Ti rich troctolites at the base (<5 vol%), and fine--grain olivine gabbros through coarse olivine gabbros, gabbronorites (<20 vol%), pyroxene gabbros and pyroxene-hornblende gabbros (>75 vol%). – Ultramafic to mafic volume ratio ~5: 95%	– Pyroxene gabbros and olivine gabbros (~80 vol%), troctolites, and hornblende gabbros with subordinate anorthosite. Except Motaghairat (lherzolites, orthopyroxenites, olivine gabbros, troctolites, and anorthosites). – Ultramafic to mafic rock volume ratio ~10: 90%	– Dunites at core enveloped by harzburgites/pyroxenites or wehrlites, where (>80vol.%) gabbronorites, hornblende gabbros and diorites at the rim . Or Cpx-rich dunite at core surrounded by hornblende--bearing lherzolites or clinopyroxenites, plagioclase hornblendites, where (>70 vol.%) norites, hornblende gabbros and diorites at the rim. – Ultramafic to mafic volume ratio ~50: 50% or ~30: 70%.	– Panzhihua: layered melanogabbro, gabbro and leucogabbro at the top. – Sept Iles: troctolite and gabbro at the base and anorthosite at the top. – Skaergaard: gabbro, ferro diorite, anorthosite and granophyre. – Bushveld: Mg-orthopyroxenites and harzburgites, followed by noritic + gabbronoritic sequences and magnetite--bearing gabbros and ferro--diorites. – Koillismaa: olivine gabbronorite, plagioclase-olivine-bronzite and gabbros and leucogabbros.
Crystallization Sequence and mineralization deposits	– Olivine(Olv)+Fe-Ti oxides+ pargasite (Prg), Olv+plagioclase (Plg)±clinopyroxene(Cpx), Olv+Plg, coarse Olv+Plag+Cpx, Plg+Cpx, Plg+ Cpx+orthopyroxene(Opx), Plg+Cpx+hornblende(Hb) – Ore deposits: highly enriched in Fe-Ti-V oxides as layers	– Um Rus (Olv, Plg, Cpx, Opx, and Hb); Um Battat (Plg, Olv, Pyx and Hb); El-Bakriya (Plg, Olv, Opx, and Cpx); Atud (Olv, Plg, Pyx and Hb); Motaghairat (Olv, Opx, Cpx, Hb and Plg). – Ore deposits: highly enriched in Fe-Ti-V oxides	– Olv + chromian spinel (Cr-Spl), Olv + Cpx, Olv + Cpx + Opx, Plg + Opx + Cpx, Plg + Hb. Or Olv + Cr-Spl, Olv + Cr--Spl + Cpx, Plg+Hb+Opx, Plg+Hb. – Ore deposits: enriched in Cu--Ni–PGE-S mineralizations	– Panzhihua: Olivine, clinopyroxene and plagioclase, and finished with amphibole, titanomagnetite, and sulfide. – Sept Iles: plagioclase and olivine, followed by magnetite and ilmenite, then Ca-rich pyroxene and finally apatite. – The Koillismaa: plagioclase, olivine, Orthopyroxene, Clinopyroxene, Magnetite. – Ores: enriched in Fe-Ti-V oxides
Crystallization temperature and oxygen fugacity	– -T: ~700 to 1100 °C – -$fO2$: FMQ +4.1 to FMQ +4.3	– Um Rus (825-931 °C); Um Battat (818.4-1036.4 °C); El-Bakriya (840-1075 °C); Motaghairat (935–1104 °C)	– Dahanib (760 °C to 1150 °C)	– Panzhihua: 1126 1176 °C – The Koillismaa: 1131–1253 °C
Age of Rocks or Complex	~740 Ma	– Um Rus (615–679 Ma); Atud (640 Ma). – Motaghairat (a relative age < 700 Ma)	– Abu Hamamid (770 ± 20 Ma (Farahat and Helmy, 2006). – Genina Gharbia (963 ± 81 Ma)	– Panzhihua: ~263 Ma; Sept Iles: ~564 Ma; Skaergaard: ~55 Ma; Bushveld: ~2060 Ma; The Koillismaa ~2440 Ma.
Magma Types and tectonic setting	– Hydrous ferropicritic melts of tholeiitic affinity – Island arc setting	– Tholeiitic to calc-alkaline magmas. – Island arc setting (Um Rus intrusion) to rift tectonic setting	– Tholeiitic melts (Abu Hamamid Genina Gharbia, Dahanib) to hydrous picritic magma (Akarem). – Island arc setting	– Panzhihua: Ferropicritic parent melts with tholeiitic affinity to high-Ti tholeiites (Ferrobasalt parent melt). – Rift related tectonic setting.

6.4. Origin of corona textures in Korab Kansi mafic-ultramafic rocks

Corona texture is one of distinctive features of cumulates formed from hydrous mafic magmas and its formation is attributed to magmatic fluids (Joesten, 1986) or metamorphic processes (Lamoen, 1979). Chemical disequilibrium between reactants is commonly suggested for the development of corona textures (Claeson, 1998; Xie et al., 2017). Corona texture is an ubiquitous feature of the Korab Kansi mafic-ultramafic intrusion where it is found in nearly all gabbroic varieties (Fig. 3e, i). It is interpreted to have formed as an intercumulus growth around early cumulus crystals. Corona texture is not only dominant in the Korab Kansi intrusion, but it is also dominant in all SED mafic-ultramafic intrusions crystallized from hydrous melts in sub-arc settings (Helmy et al., 2008; Abdel Halim et al., 2016; Khedr and Arai, 2016a, 2016b). The observed types of a corona structure in the Korab Kansi intrusion are: 1) thin rims of orthopyroxene between olivine and plagioclase, recorded only in olivine gabbros (Fig. 3e); and 2) rims of pargasite of variable thicknesses at contacts between either olivine, Cpx or ilmenite and plagioclase (Fig. 3e–h), and also between olivine and ilmenite. Pargasite grains grew at the expense of cumulus phases (e.g. plagioclase and olivine) as a result of a reaction between the interstitial magmatic liquid (e.g. hydrous oxide-rich silicate melt; Irvine, 1980) and cumulus phases (Xie et al., 2017).

The dominance of amphibole corona in the Korab Kansi intrusion reflects the hydrous nature of the parental magma (Helmy et al., 2008; Khedr and Arai, 2016b). Compositions of reactant and physiochemical conditions control mineral diversity, where amphibole is more stable at high P_{H2O} relative to clinopyroxene, but orthopyroxene is more stable at high temperatures. Furthermore, fractionation increases H_2O content in the residual melt phase, which leads to the development of thicker coronas and intercumulus pargasite in more fractionated rocks (e.g. pyroxene-hornblende gabbros; Fig. 3k). Orthopyroxene corona formed during reaction between evolved trapped melts and cumulus olivine and plagioclase in olivine gabbros at high temperature, similar to the

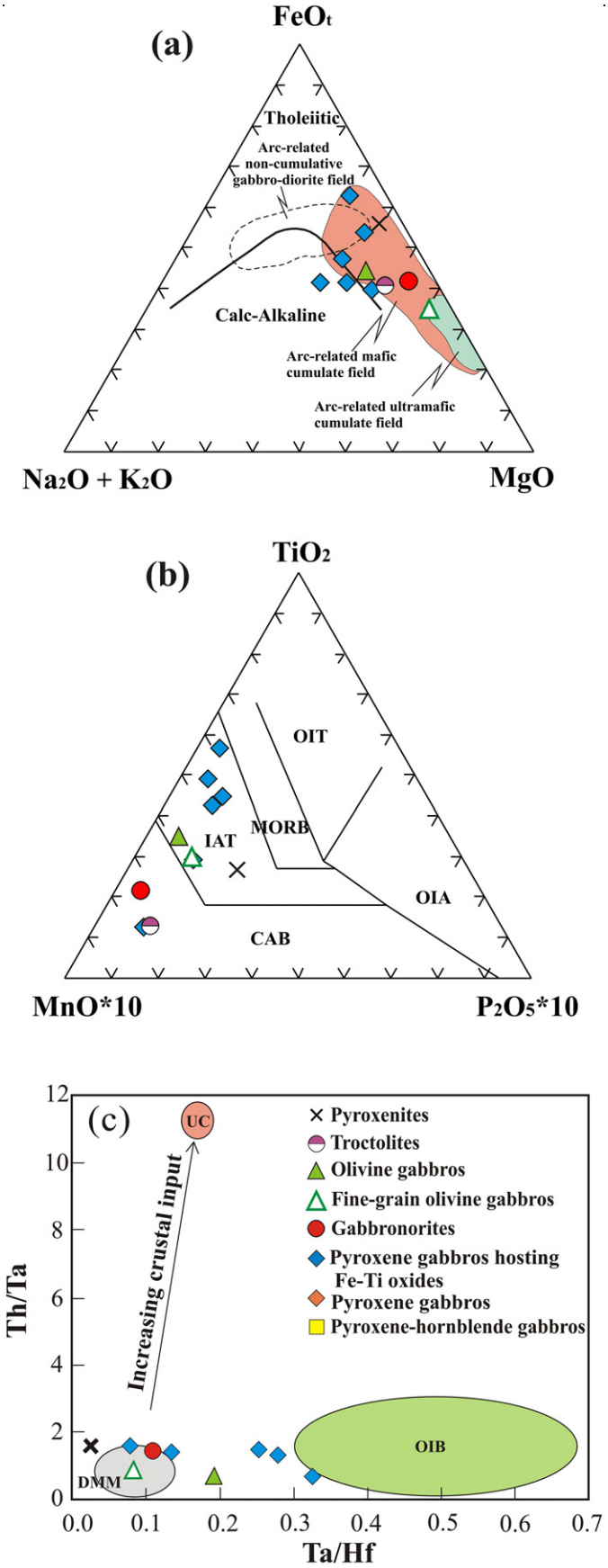

formation of orthopyroxene coronas in the Ji'nan layered mafic/ultramafic intrusion (Xie et al., 2017). This corona texture is attributed to an increase in the activity of silica during fractional crystallization through the reaction olivine + SiO_2 = orthopyroxene (Nishiyama, 1983).

6.5. Why is the Korab Kansi intrusion enriched in Fe-Ti oxides?

The economic Fe-Ti oxide ore layers hosted in the Korab Kansi intrusion (Fig. 2a, b) indicate significant Fe-Ti enrichment of its parent magma.

The type of parental magmas is an important factor in forming Fe-Ti oxide deposits. Parent magmas that are enriched in Fe and Ti are produced either directly from partial melting of a Fe-Ti rich mantle source or as a result of tholeiitic-trend differentiation of mantle-derived magma that enriches Fe and Ti (Pang et al., 2008). The association of Fe-Ti oxides with more primitive rocks of the Korab Kansi intrusion (e.g. dunites and troctolites; Fig. 3a, e, f) suggest that fractional crystallization of Fe-Ti rich parental magma was responsible. This is similar to the model used to explain formation of Fe-Ti-V oxides-rich rocks of the Skaergaard intrusion (Reynolds, 1985) and Fe-rich oxides of the Bushveld (Scoon and Mitchell, 1994). The parent magma composition thus was the main factor controlling deposition of Fe-Ti rich layers in the Korab Kansi intrusion (Figs. 2a–b, 3a, d, f, h).

Ferrobasaltic and ferropicritic magmas favor the formation of Fe-Ti oxides. The ferropicritic parental magma suggested for the Korab Kansi mafic-ultramafic intrusion represents primitive Fe-rich mantle-derived melts (Gibson et al., 2000). The origin of ferropicrites could be attributed to high pressure partial melting of peridotite–eclogite (pyroxenite) mixture that possibly incorporated recycled oceanic crust components (Desta et al., 2014) or to partial melting of Si-deficient pyroxenite at high temperatures (Jennings et al., 2016). The existence of peridotites and pyroxenites (Figs. 2, 3a-e) in the Korab Kansi intrusion supports this model for the origin of ferropicrites. Experiments of Langmuir and Hanson (1980) indicate that Fe concentration increases with increased partial melting at high pressure (P) and temperature (T). The crystallization pressure of the Korab Kansi intrusion is mostly below 5 Kbar (Fig. 8) to form large amounts of olivine-rich cumulates (Fig. 3a), after fractionation and enrichment of Fe and Ti of its parental magma at deeper mantle depths at high pressure. The interaction of Nubian metasomatized lithosphere with asthenospheric melts could also have been responsible for Fe and Ti enrichment of Korab Kansi ferropicritic parental melts (see section 6.3). The generation of Ti-rich parental melts and formation of Fe-Ti deposits in some Egyptian layered intrusions possibly reflect Ti enrichment as a result of mantle metasomatism accompanying upwelling asthenospheric melts and/or recycled oceanic crust (Jennings et al., 2016) in the presence of slab-derived melts/fluids (Figs. 5–7), causing mantle heterogeneity during formation of the Nubian Shield.

The oxygen fugacity (Fig. 11) and H_2O content of Korab Kansi magma were other important factors controlling precipitation of large quantities of Fe-Ti oxides (Kress and Carmichael, 1991). The crystallization of Fe-Ti oxides in large amounts requires high fO_2 (Howarth and Prevec, 2013) and implies high magmatic water contents (see Section 6.2). This condition is expected for the island-arc setting of the Korab Kansi intrusion, where slab-derived melts/fluids are important. Moreover, experiments of Toplis and Carroll (1995) revealed that crystallization of Fe-Ti oxides at low pressures is favored by more oxidizing conditions. The crystallization interval during which Fe-Ti oxides crystallize depends strongly on magma system conditions, especially fO_2 (Toplis and Carroll, 1995). The high fO_2 and H_2O contents of the parent

Fig. 13. Whole-rock chemistry showing tectonic setting of the Korab Kansi intrusion. **a**) Y/15-La/10-Nb/8 ternary diagram (Cabanis and Lecolle, 1989) for the studied mafic-ultramafic rocks. **b**) TiO_2-MnO*10-P_2O_5*10 ternary diagram (after Mullen, 1983) for the studied mafic-ultramafic rocks, **c**) Ta/Hf vs Th/Ta diagram (Manya, 2014) for the mafic-ultramafic rocks.

magma caused early crystallization of Fe-Ti oxides (e.g., Ganino et al., 2008). Consequently, high fO_2 (Fig. 11) and H_2O contents of the Korab Kansi parent ferropicritic magma significantly reduce the silicate stability field, causing Fe-Ti oxides to crystallize with olivine (Fig. 3a), before plagioclase and clinopyroxene crystallized (e.g., Howarth and Prevec, 2013). The highly oxidizing magmatic conditions, evidenced by ilmenite with high V_2O_5 (~3.8 wt% on average; Supplementary 3), and the parental Ti-rich ferropicritic melts can explain why the Korab Kansi intrusion is rich in Fe-Ti oxides/deposits compared with other Cu–Ni-PGE-rich intrusive complexes in the Eastern Desert of Egypt (Fig. 1a). The low amounts of sulphides associated with Fe-Ti oxides in the Korab Kansi intrusion may be attributed to oxygen consumption during oxide crystallization that may force sulfide precipitation to buffer oxygen fugacities (Mathez, 1976). On the other hand, it is noted that Fe-Ti oxide-rich gabbros (e.g. samples Kn.2, Kn.4, Kn.15, kn. 41) are highly enriched in LREE relative to HREE compared with the remaining Fe-Ti oxide-poor gabbroic samples (Table 3), suggesting the role of fluid mobile elements (e.g., LREE) in mobility and collection of titanomagnetite-ilmenite grains if the parent melts are rich in the Fe and Ti oxides.

7. Concluding remarks

In conclusion, based on field relation (Fig. 2), petrography (Fig. 3) and mineral chemistry (Figs. 4–9), Korab Kansi parent ferropicrite melts were derived from extensive partial melting of Ti- and Fe-rich upper mantle that had been modified by melts/fluids from subducted oceanic crust. Parental melts are best approximated by fine-grained olivine gabbros. The crystallization sequence was olivine, Fe-Ti oxides, plagioclase, clinopyroxene, hornblende, and orthopyroxene, forming different igneous layers (Table 4; Figs. 4, 14). The magmatic processes and formation of the Korab Kansi ultramafic-mafic rocks can be summarized as follows (Fig. 14): 1) Ferropicrite melts fractionated in the upper mantle to form the chromite-dunite complex due to reaction between primitive melts and mantle peridotites; 2) Slightly fractionated melts after crystallization of chromite-dunite crystallized to form hornblende dunites (1100 °C, 5 Kbar and depth ~15 km; Fig. 8) and Cr-free cumulate dunites, with abundant intercumulus titanomagnetite-ilmenites (Fig. 3a), forming Fe-Ti oxide layers (Figs. 2a, b, h; 14); 3) These dunites are associated with dykes of Fe-Ti rich hornblendes, pyroxenites and troctolites (ultramafic zone, Fig. 14) because of the enrichment of Fe and Ti during melt fractionation; 4) Some quenched melts, similar in chemistry to ferropicrites, crystallized to form fine-grained olivine gabbros in the marginal zone (Fig. 14) and other gabbroic rocks (coarse olivine gabbros, gabbronorite, pyroxene gabbros and hornblende pyroxene gabbros, respectively; Fig. 14) during upward migration of melts; 5) The fractionation occurred at higher pressures in a deeper depth, and solidification of fractionated magmas occurred at lower pressures (Fig. 14) in order to form voluminous olivine-rich cumulate (Fig. 3). The fractionated magma crystallized from the bottom to roof, forming different igneous layers (Fig. 2c), cumulate textures (Fig. 3a, c, e) and Fe-Ti rich oxide layers (Fig. 2a, b, h) during igneous processes including magma differentiation and fractional crystallization; 6) The Fe

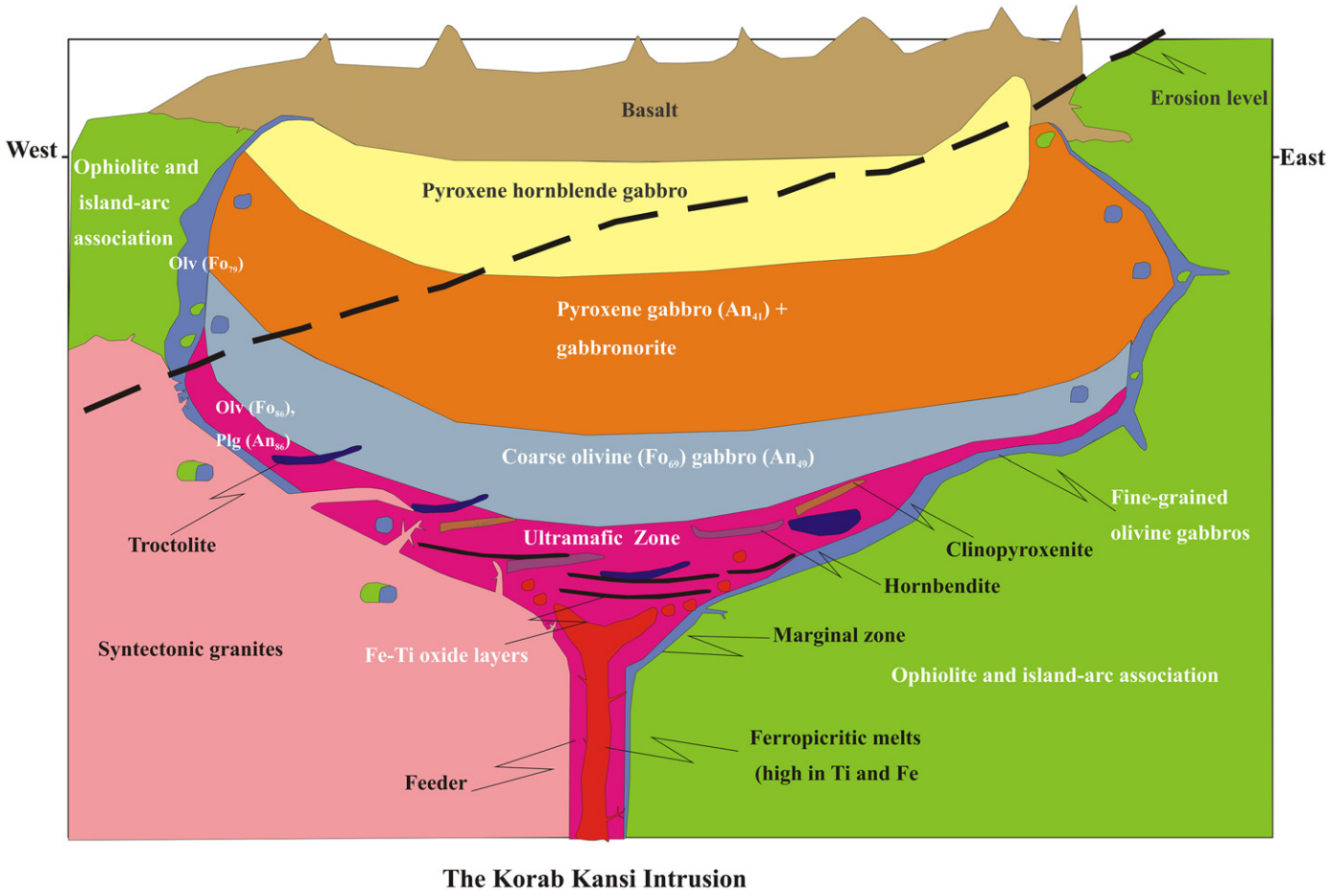

Fig. 14. Simplified section of the Korab Kansi intrusion toward down dip showing a layered igneous intrusion. The ferropicritic magma crystallized from the bottom to upward (roof), forming different igneous layers during igneous processes including magma differentiation and fractional crystallization. The intrusion is characterized by cumulate layers and cumulate textures of crystallizing minerals started with olivine, Fe-Ti rich oxides, plagioclase, clinopyroxene, hornblende, and orthopyroxene, respectively. The fine-grained olivine gabbros crystallized in the marginal zone and may represent quenched melts approximating primary magma compositions. The dotted line is the erosion level. Plagioclase anorthite content (Plg An) and olivine forsterite content (Olv Fo) are shown to indicate a fractional-crystallization sequence.

and Ti-rich nature of ferropicritic melts and high oxygen fugacity and H_2O contents of these parental melts were key factors for enriching Fe-Ti oxides in the Korab Kansi intrusion. The other factors possibly controlling the Fe-Ti oxide ores hosted in this intrusion are mixed melts resulting from the interaction of metasomatized lithospheric mantle with upwelling asthenospheric melts; 7) Further study is needed to reveal whether the intrusion formed as a result of a single episode of magma intrusion or multiple cycles of magma influx, fractional crystallization, and remixing of residual magma with primitive magma. Further studies are needed to address whether the Korab Kansi intrusion fed a volcano or not. Further studies are needed to compare Korab Kansi parental magma compositions and crystallization sequence with other Cryogenian – Tonian intrusions of the SE Desert of Egypt and to test the idea that Alaskan-type intrusions are enriched in PGEs whereas layered intrusions of similar age are enriched in Fe-Ti-V deposits.

Supplementary data to this article can be found online at https://doi.org/10.1016/j.gr.2019.12.013.

Declaration of competing interest

The authors declare that they have no known competing financial interests or personal relationships that could have appeared to influence the work reported in this paper.

Acknowledgments

The authors thank the Shalateen Company of Mineral Resources for giving permission (March to May, 2018) to study the Korab Kansi area. The first and second authors are grateful for the help of Ahmed Abu Al-Azayem Al Desouky and Adroob Said during field work in the Korab Kansi area and staying in Shalateen city. Walter Goessler is thanked for ICPMS analysis of whole rock samples. We thank Saif Abu Khashaba for preparing Landsat maps of the Korab Kansi area. We are grateful to anonymous reviewers for their beneficial comments. We thank M. Santosh for his editorial handling of this manuscript.

References

Abdel Halim, A.H., Helmy, H.M., Abd El-Rahman, Y.M., Shibata, T., El Mahallawi, M.M., Yoshikawa, M., Arai, S., 2016. Petrology of the Motaghairat mafic-ultramafic complex, Eastern Desert, Egypt: a high-Mg post-collisional extension-related layered intrusion. Journal of Asian Earth Sciences 116, 164–180.

Abdel-Gawad, G.M., 2002. Geological and geochemical characteristics of the mafic-ultramafic rocks of Gabal Korab Kansi area, South Eastern Desert, Egypt. Ph.D. Zagazig University, Thesis, p. 195.

Abu Anbar, M.M., 2001. Petrology and mineralogy of Umm Rus Gabbroic intrusion, Eastern Desert, Egypt. Egyptian Journal of Geology 45 (1B), 445–472.

Abu El Ela, A.M., 1991. A petrological study on the gabbroic rocks of the Um Rus and Atud intrusions, Eastern Desert, Egypt. Delta Journal of Science 15, 204–246.

Ali, K.A., Stern, R.J., Manton, W.I., Kimura, J.-I., Khamis, H.A., 2009. Geochemistry, Nd isotopes, and U-Pb SHRIMP zircon dating of neoproterozoic volcanic rocks from the Central Eastern Desert of Egypt: new insights into the 750 Ma crust-forming event. Precambrian Research 171, 1–22.

Atkin, F.B., 1969. Pyroxenes of the Bushveld intrusion, South Africa. Journal of Petrology, Oxford 10, 222–249.

Azer, M.K., El-Gharbawy, R.I., 2011. Contribution to the Neoproterozoic layered mafic-ultramafic intrusion of Gabal Imleih, south Sinai, Egypt: implication of post-collisional magmatism in the north Arabian-Nubian Shield. Journal of African Earth Sciences 60, 253–272.

Azer, M.K., Obeid, M.A., Gahlan, H.A., 2016. Late Neoproterozoic layered mafic intrusion of arc-affinity in the Arabian-Nubian Shield: a case study from the Shahira layered mafic intrusion. Geologica Acta 14, 237–259.

Bai, Z.J., Zhong, H., Naldrett, A.J., Zhu, W.G., Xu, G.W., 2012. Whole-rock and mineral composition constraints on the genesis of the giant Hongge Fe-Ti-V oxide deposit in the Emeishan Large Igneous Province, Southwest China. Economic Geology 107, 507–524.

Ballhaus, C., Berry, R.F., Green, D.H., 1990. Oxygen fugacity controls in the Earth's upper mantle. Nature 348, 437–440.

Ballhaus, C., Berry, R.F., Green, D.H., 1991. High pressure experimental calibration of the olivine-orthopyroxene-spinel oxygen geobarometer: implications for the oxidation state of the upper mantle. Contributions to Mineralogy and Petrology 107, 27–40.

Be'eri-Shlevin, Y., Katzir, Y., Whitehouse, M., 2009. Post-collisional tectonomagmatic evolution in the northern Arabian–Nubian Shield: time constraints from ion-probe U-Pb dating of zircon. Geological Society of London 166, 71–85.

Beard, J.S., 1986. Characteristic mineralogy of arc-related cumulate gabbros: implications for the tectonic setting of gabbroic plutons and for andesite genesis. Geology 14, 848–851.

Beccaluva, L., Maccoita, G., Piccardo, G.B., Zeda, O., 1989. Clinopyroxene composition of ophiolite basalts as petrogenetic indicator. Chemical Geology 77, 165–182.

Bédard, E., Hébert, R., Guilmette, C., Lesage, G., Wang, C.S., Dostal, J., 2009. Petrology and geochemistry of the Saga and Sangsang ophiolitic massifs, Yarlung Zangbo Suture Zone, Southern Tibet: evidence for an arc–back-arc origin. Lithos 113, 48–67.

Bence, A.E., Albee, A.L., 1968. Empirical correction factors for the electron microanalysis of silicates and oxides. Journal of Geology 76, 382–403.

Blundy, J.D., Holland, T.J.B., 1990. Calcic amphibole equilibria and a new amphibole-plagioclase geothermometer. Contributions to Mineralogy and Petrology 104, 208–224.

Brey, G.P., Kohler, T., 1990. Geothermobarometry in four-phase lherzolites II. New thermobarometers, and practical assessment of existing thermobarometers. Journal of Petrology 31, 1353–1378.

Brown, E., 1977. The crossite content of Ca-amphibole as a guide to pressure of metamorphism. Journal of Petrology 18, 53–72.

Bunch, T.E., Okrusch, M., 1973. Al-rich pargasite. American Mineralogist 58, 721–726.

Cabanis, B., Lecolle, M., 1989. Le diagramme La/10-Y/15-Nb/8: Un outil pour la discrimination des series volcaniques et la mise en evidence des processus de mélange et/ou de contamination crustale: Comptes Rendus de l'Académie des Sciences–Series IIA–Earth and. Planetary Science 309, 2023–2029.

Cao, J., Wang, C.Y., Xing, C.-M., Xu, Y.-G., 2014. Origin of the early Permian Wajilitag igneous complex and associated Fe–Ti oxide mineralization in the Tarim large igneous province, NW China. Journal of Asian Earth Sciences 84, 51–68.

Claeson, D.T., 1998. Coronas, reaction rims, symplectites and emplacement depth of the Rymmen gabbro, Transscandinavian Igneous Belt, southern Sweden. Mineralogical Magazine 62, 743–757.

Claeson, D.T., Meurer, W.P., 2004. Fractional crystallization of hydrous basaltic "arc-type" magmas and the formation of amphibole-bearing gabbroic cumulates. Contribution to. Mineralogy and Petrology 147, 288–304.

DeBari, S.M., Coleman, R.G., 1989. Examination of the deep levels of an island arc: evidence from the Tonsina ultramafic–mafic assemblage, Tonsina, Alaska. Journal of Geophysical Research 94, 4373–4391.

Deer, W.A., Howie, R.A., Zussman, J., 1992. An introduction to the rock forming minerals. 2nd ed. Longman, Scientific and Technical, London 696 p.

Desta, M.T., Ayalew, D., Ishiwatari, A., Arai, S., Tamura, A., 2014. Ferropicrite from the lalibela area in the Ethiopian large igneous province. Journal of Mineralogical and Petrological Sciences 109, 191–207.

Dong, H., Xing, C., Wang, C.Y., 2013. Textures and mineral compositions of the Xinjie layered intrusion, SW China: Implications for the origin of magnetite and fractionation process of Fe-Ti-rich basaltic magmas. Geoscience Frontiers 4, 503–515.

EL-Kazzaz, Y.A., 2012. Shear zones related gold-bearing quartz veins in Shinai area, South Eastern Desert. Egypt. Egyptian Journal of Geology 56, 67–89.

El-Ramly, M.F., 1972. A new geological map for the basement rocks in the Eastern and Southwestern Deserts of Egypt. Annals of the Geological Survey of Egypt, Cairo 2, 1–18.

Erdenesaihan, G., Ishiwatari, A., Orolmaa, D., Arai, S., Tamura, A. 2014. Discovery of ferropicrites and high-magnesian andesites from the Erdenetsogt formation, central mongolia. Proceedings of the Mongolian Academy of Sciences 54, No 04 (212). doi: https://doi.org/10.5564/pmas.v54i4.625

Essawy, M.A., El-Metwally, A.A., Althaus, E., 1997. Pan-African layered mafic-ultramafic-mafic cumulate complex in the SW Sinai massif: mineralogy. geochemistry and crustal growth. Chemie der Erde 57, 137–156.

Farahat, E.S., Helmy, H.M., 2006. Abu Hamamid Neoproterozoic Alaskan-type complex, south Eastern Desert, Egypt: petrogenetic and geotectonic implications. African Earth Sciences 85, 187–197.

Fazlnia, N., Alizade, A., 2013. Petrology and geochemistry of the Mamakan gabbroic intrusions, Urumieh (Urmia), Iran: magmatic development of an intra-oceanic arc. Periodico di Mineralogia 82 (2).

Fiala, J., Ulrych, J., Lang, M., Pivec, E., 1975. Coexistence of the principle minerals of the Pecerady gabbro (in Czeck). Studie CSAV12 141–160.

Fiorentini, M.L., Beresford, S.W., Deloule, E., Hanski, E., Stone, W.E., Pearson, N.J., 2008. The role of mantle-derived volatiles in the petrogenesis of Palaeoproterozoic ferropicrites in the Pechenga Greenstone Belt, northwestern Russia: Insights from in-situ microbeam and nanobeam analysis of hydromagmatic amphibole. Earth and Planetary Science Letters 268, 2–14.

Fleet, M.E., Barnett, R.L., 1978. $Al_{(iv)}/Al_{(vi)}$ partitioning in calciferous amphiboles from the mine, Sudbury, Ontario. Canadian Mineralogist 16, 527–532.

Frost, D.J., 2006. The stability of hydrous mantle phases. Reviews in Mineralogy and Geochemistry 62, 243–271.

Ganino, C., Arndt, N.T., Zhou, M.F., Gaillard, F., Chauvel, C., 2008. Interaction of magma with sedimentary wall rock and magnetite ore genesis in the Panzhihua mafic intrusion, SW China. Mineralium Deposita 43, 677–694.

Ghoneim, M.F., 1988. Mineral chemistry of some gabbroic rocks of the central Eastern Desert. Egypt. Chemie der Erde 48, 191–201.

Gibson, S.A., Thompson, R.N., Dickin, A.P., 2000. Ferropicrites: geochemical evidence for Fe–rich streaks in upwelling mantle plumes. Earth and Planetary Science Letters 174, 355–374.

Girardeau, J., Mevel, C., 1982. Amphibolitized sheared gabbros from ophiolites as indicators of the evolution of the oceanic crust: Bay of Islands, Newfoundland. Earth Planetary Science Letter 61, 151–165.

GSE, 2002. Geological Map of Marsa Sha'ab Quadrangle, South Eastern Desert, Egypt: Scale 1: 250,000. The Egyptian Mineral Resources Authority. Cairo, Egypt.

Hart, S.R., Dunn, T., 1993. Experimental Cpx/melt partitioning of 24 trace elements. Contributions to Mineralogy and Petrology 113, 1–8.

Haskin, L.A., Salpas, P.A., 1992. Genesis of compositional characteristics of Stillwater AN-I and AN-II thick anorthosite units. Geochimica et Cosmochimica Acta 56, 1187–1212.
Helmy, H.M., 2004. Cu-Ni-PGE mineralization in the Genina Gharbia mafic-ultramafic intrusion, Eastern Desert. Egypt. Canadian Mineralogist 42, 351–370.
Helmy, H.M., El Mahallawi, M.M., 2003. Gabbro Akarem mafic– ultramafic complex, Eastern Desert, Egypt: a Late Precambrian analogue of Alaskan-type complexes. Mineralogy and Petrology 77, 85–108.
Helmy, H.M., Mogessie, A., 2001. Gabbro Akarem, Eastern Dessert, Egypt: Cu-Ni-PGE mineralization in a concentrically zoned mafic–ultramafic complex. Mineralium Deposita 36, 58–71.
Helmy, H.M., Yoshikawa, M., Shibata, T., Arai, S., Tamura, A., 2008. Corona structure from arc mafic-ultramafic cumulates: the role and chemical characteristics of late-magmatic hydrous liquids. Journal of Mineralogical and Petrological Sciences 103, 333–344.
Helmy, H.M., Abd El-Rahman, Y.M., Yoshikawa, M., Shibata, T., Arai, S., Tamura, A., Kagami, H., 2014. Petrology and Sm-Nd dating of the Genina Gharbia Alaskan-type complex (Egypt): insights into deep levels of Neoproterozoic island arcs. Lithos 198–199, 263–280.
Helmy, H.M., Yoshikawa, M., Shibata, T., Arai, S., Kagami, H., 2015. Sm-Nd dating and petrology of Abu Hamamid intrusion, Eastern Desert, Egypt: a case of Neoproterozoic Alaskan-type complex in a back arc setting. Precambrian Research 258, 234–246.
Helz, R.T., 1973. Phase relation of basalt in their melting range at $P_{H2O} = 5$ kb. As a function of oxygen fugacity. Part1. mafic phases. Journal of Petrology 14, 249–302.
Hill, R., Roeder, P., 1974. The crystallization of spinel from basaltic liquid as a function of oxygen fugacity. Journal of Geology 82, 709–729.
Himmelberg, G.R., Loney, R.A., 1995. Characteristics and petrogenesis of Alaskan-type ultramafic–mafic intrusions. Southeastern Alaska. U.S. Geological Survey Professional Paper 1564.
Howarth, G.H., Prevec, S.A., 2013. Hydration vs. oxidation: Modelling implications for Fe-Ti oxide crystallization in mafic intrusions, with specific reference to the Panzhihua intrusion, SW China. Geoscience Frontiers 4, 555–569.
Hynes, A., 1982. A comparison of amphiboles from medium and low pressure metabasites. Contributions to Mineralogy and Petrology 81, 119–125.
Irvine, N.T., 1980. Magmatic infiltration metasomatism, double diffusive fractional crystallization, and adcumulus growth in the Muskox intrusion and other layered intrusions. In Physics of magmatic processes (Hargraves, R.B. Ed.). Princeton University Press, Princeton, 325-383.
Jang, Y.D., Naslund, H.R., 2003. Major and trace element variation in ilmenite in the Skaergaard Intrusion: petrologic implications. Chemical Geology 193, 109–125.
Jang, Y.D., Naslund, H.R., McBirney, A.R., 2001. The differentiation trend of the Skaergaard intrusion and the timing of magnetite crystallization: iron enrichment revisited. Earth and Planetary Science Letters 189, 189–196.
Jennings, E.S., Holland, T.J., Shorttle, O., Maclennan, J., Gibson, S.A., 2016. The composition of melts from a heterogeneous mantle and the origin of ferropicrite: application of a thermodynamic model. Journal of Petrology 57, 2289–2310.
Jiang, C.Y., An, S.Y., 1984. On chemical characteristics of calcic amphiboles from igneous rocks and their petrogenesis significance (in Chinese with English abstract). Journal of Mineralogy and Petrology 3, 1–9.
Joesten, R., 1986. The role of magmatic reaction, diffusion and annealing in the evolution of coronitic microstructures in troctolitic gabbros from Risør, Norway. Mineralogical Magazine 50, 441–467.
Johnson, K.T.M., 1998. Experimental determination of partition coefficients for rare earth and high field strength elements between clinopyroxene, garnet and basaltic melt. Contributions to Mineralogy and Petrology 133, 60–68.
Juster, T.C., Grove, T.L., Perfit, M.R., 1989. Experimental constraints on the generation of Fe-Ti basalts, andesites, and rhyodacites at the Galapagos Spreading Centre, 85°W and 95°W. Journal of Geophysical Research 94, 9251–9274.
Karinen, T., 2010. The Koillismaa Intrusion, northeastern Finland –evidence for PGE reef forming processes in the layered series. Geological Survey of Finland, Bulletin 404, 1–176.
Khedr, M.Z., Arai, S., 2010. Hydrous peridotites with Ti-rich chromian spinel as a low temperature forearc mantle facies: evidence from the Happo-O'ne metaperidotites (Japan). Contributions to Mineralogy and Petrology 159, 137–157.
Khedr, M.Z., Arai, S., 2013. Origin of Neoproterozoic ophiolitic peridotites in south Eastern Desert, Egypt, constrained from primary mantle mineral chemistry. Mineralogy and Petrology 107, 807–828.
Khedr, M.Z., Arai, S., 2016a. Chemical variations of mineral inclusions in Neoproterozoic high-Cr chromitites from Egypt: evidence of fluids during chromitite genesis. Lithos 240–243, 309–326.
Khedr, M.Z., Arai, S., 2016b. Petrology of a Neoproterozoic Alaskan-type complex from the Eastern Desert of Egypt: implications for mantle heterogeneity. Lithos 263, 15–32.
Khedr, M.Z., Arai, S., 2017. Peridotite-chromitite complexes in the Eastern Desert of Egypt: Insight into Neoproterozoic sub-arc mantle processes. Gondwana Research 52, 59–79.
Khedr, M.Z., Arai, S., Tamura, A., Morishita, T., 2010. Clinopyroxenes in high-P metaperidotites from Happo-O'ne, central Japan: implications for wedge-transversal chemical change slab-derived fluids. Lithos 119, 439–456.
Khedr, M.Z., Arai, S., Python, M., Tamura, A., 2014. Chemical variations of abyssal peridotites in the central Oman ophiolite: evidence of oceanic mantle heterogeneity. Gondwana Research 25, 1242–1262.
Khudeir, A.A., 1995. El-Genina El-Gharbia and El-Genina El-Sharkia ultramafic-mafic intrusions, Eastern Desert, Egypt: geology, petrology, geochemistry and petrogenesis. Assiut University, Bulletin of Faculty Sciences 2-F, 177–219.
Kress, V.C., Carmichael, I.S.E., 1991. The compressibility of silicate liquids containing Fe_2O_3, and the effect of composition, temperature, oxygen fugacity and pressure on their redox states. Contributions to Mineralogy and Petrology 108 (1-2), 82–92.
Kröner, A., Todt, W., Hussein, I.M., Mansour, M., Rashwan, A.A., 1992. Dating of late Proterozoic ophiolites in Egypt and the Sudan using the single grain zircon evaporation technique. Precambrian Research 59, 15–32.
Lamoen, H., 1979. Coronas in olivine gabbros and iron ores from Susimaki and Riuttamaa. Finland. Contributions to Mineralogy and Petrology 68, 259–268.
Langmuir, C.H., Hanson, G.N., 1980. An evaluation of major element heterogeneity in the mantle sources of basalts. Philosophical Transactions of the Royal Society of London, Series A 297, 383–407.
Le Bas, N.J., 1962. The role of aluminum in igneous clinopyroxenes with relation to their parentage. American Journal of Science 260, 228–267.
Leake, et al., 1997. Nomenclature of amphiboles: Report of the subcommittee on amphiboles of the international mineralogical association, commission on new minerals and mineral names. American Mineralogist 82, 1019-1037.
Leterrier, J., Maury, R.C., Thonon, P., Girard, D., Marchal, M., 1982. Clinopyroxene composition as a method of identification of the magmatic affinities of paleo-volcanic series. Earth and Planetary Science Letters 59, 139–154.
Loftus-Hills, G., Solomon, M., 1967. Cobalt, nickel and selenium in sulphides as indicators of ore genesis. Mineralium Deposita 2, 228–242.
Loucks, R.R., 1990. Discrimination of ophiolitic from nonophiolitic ultramafic-mafic allochthons in orogenic belts by the Al/Ti ratio in clinopyroxene. Geology 18, 346–349.
Makhlouf, A., Beniamin, N.Y., Mansour, M.M., Mansour, S.A., El-Shrbeni, H., 2008. Mafic-ultramafic intrusion of South Korab Kansi area with emphasis on titanomagnetite ores, south Eastern Desert, Egypt. Annals of the Geological Survey of Egypt V.XXX 1–20.
Manya, S., 2014. Geochemistry of the Palaeoproterozoic gabbros and granodiorites of the Saza area in the Lupa Goldfield, southwestern Tanzania. Journal of African Earth Sciences 100, 401–408.
Mao, J.W., Pirajno, F., Zhang, Z.H., Chai, F.M., Wu, H., Chen, S.P., Cheng, L.S., Yang, J.M., Zhang, C.Q., 2008. A review of the Cu-Ni sulfide deposits in the Chinese Tianshan and Altay orogens (Xinjiang Autonomous Region, NW China): principal characteristics and ore-forming processes. Journal of Asian Earth Sciences 32, 184–203.
Mathez, E.A., 1976. Sulfur solubility and magmatic sulfides in submarine basalt glass. Journal of Geophysical Research 81, 4269–4276.
McDonough, W.F., Sun, S.S., 1995. The composition of the Earth. Chemical Geology 120, 223–253.
Morimoto, N., Fabries, J., Ferguson, A.K., Ginzburg, I.V., Ross, M., Seifert, F.A., Zussman, J., Gottardi, D., 1988. Nomenclature of pyroxenes. American Mineralogist 62, 53–62.
Mullen, E.D., 1983. $MnO/TiO_2/P_2O_5$. A minor element discriminates for petrogenesis. Earth and Planetary Science Letters 62, 53–62.
Nasr, B.B., Sadek, M.F., Masoud, M.S., 2000. Some new occurrences of layered titanomagnetite. Egypt. Annals of the Geological Survey of Egypt V.XXXIII, Eastern Desert, pp. 679–690.
Namur, O., Charlier, B., Toplis, M.J., Higgins, M.D., Liegeois, J., Pgeois, J.P., Vander Auwera, J., 2010. Crystallization sequence and magma chamber processes in the ferrobasaltic sept iles layered intrusion, Canada. Journal of Petrology 51, 1203–1236.
Nisbet, E.G., Pearce, J.A., 1977. Clinopyroxene composition in mafic lavas from different tectonic settings. Contribution to Mineralogy and Petrology 63, 149–160.
Nishiyama, T., 1983. Steady state diffusion model for olivine-plagioclase corona growth. Geochimica et Cosmochimica Acta 47, 194–283.
Norman, M., Garcia, M.O., Pietruszka, A.J., 2005. Trace-element distribution coefficients for pyroxenes, plagioclase, and olivine in evolved tholeiites from the 1955 eruption of Kilauea Volcano, Hawai'i, and petrogenesis of differentiated rift-zone lavas. American Mineralogist 90, 888–899.
Pang, K.N., Zhou, M.F., Lindsley, D., Zhao, D., Malpas, J., 2008. Origin of Fe-Ti oxide ores in mafic intrusions: evidence from the Panzhihua intrusion, SW China. Journal of Petrology 49, 295–313.
Pearce, J.A., Parkinson, I.J., 1993. Trace element model for mantle melting: application to volcanic arc petrogenesis. In: Prichard, H.M., Alabaster, T., Harris, N.B., Neary, C.R. (Eds.), Magmatic Process and Plate Tectonics. Geological Society, London, pp. 373–403 Special Publication 76.
Perchuk, L.L., 1970. Equilibria of rock-forming minerals. Moscow, Nauka, p. 320.
Perfit, M.R., Gust, D.A., Bence, A.E., Arculus, R.J., Taylor, S.R., 1980. Chemical Characteristics of Island-Arc Basalts- Implications for Mantle Sources. Chemical Geology 30, 227–256.
Piercey, S.J., Murphy, D.C., Mortensen, J.K., Creaser, R.A., 2004. Mid-Paleozoic initiation of the northern Cordilleran marginal back-arc basin: Geological, geochemical and neodymium isotopic evidence from the oldest mafic magmatic rocks in Yukon-Tanana terrane, Finlayson Lake district, southeast Yukon, Canada. Geological Society of America Bulletin 116, 1087–1106.
Pirajno, F., 2004. Hotspots and mantle plumes: global intraplate tectonics, magmatism and ore deposits. Journal of Mineralogy and Petrology 82, 183–216.
Plank, T., Kelley, K., Zimmer, A., Hauri, M.M., Wallace, E.H.P.J., 2013. Why do mafic magmas contain ~4 wt.% water on average? Earth and Planetary Science Letters 364, 168–179.
Reynolds, I.M., 1985. The nature and origin of titaniferous magnetite-rich layers in the upper zone of the Bushveld complex: a review and synthesis. Economic Geology 80, 1089–1108.
Ryan, J.G., Morris, J., Tera, F., Leeman, W.P., Tsvetkov, A., 1995. Cross-arc geochemical variations in the Kurile Arc as a function of slab depth. Science 270, 625–627.
Sadek, M.F., 1994. Geology, geochemistry and structure of Gabal Muqsium area and environs, South Eastern Desert, Egypt. Phd Thesis. Ain Shams University. Cairo, Egypt.
Schulling, R.D., Feenstra, A., 1980. Geochemical behavior of vanadium in iron-titanium oxides. Chemical Geology 30, 143–150.
Scoon, R.N., Mitchell, A.A., 1994. Discordant iron-rich ultramafic pegmatites in the Bushveld Complex and their relationship to iron-rich intercumulus and residual liquids. Journal of Petrology 35, 881–917.

Sisson, T.W., Grove, T.L., 1993. Experimental investigations of the role of H_2O in calc-alkaline differentiation and subduction zone magmatism. Contributions to Mineralogy and Petrology 113, 143–166.
Stern, R.J., Hedge, C.E., 1985. Geochronologic constraints on late Precambrian crustal evolution in the Eastern Desert of Egypt. American Journal of Science 285, 7–127.
Stern, R.J., Kroner, A., Manton, W.I., Reischmann, T., Mansour, M., Hussein, I.M., 1989. Geochronology of the late Precambrian Hamisana shear zone, Red Sea Hills. Sudan and Egypt. Journal of the Geological Society, London 146, 1017–1030.
Stern, R.J., Kröner, A., Rashwan, A.A., 1991. A late Precambrian (~710 Ma) high volcanicity rift in the South Eastern Desert of Egypt. Geologische Rundschau 80, 155–170.
Stern, R.J., Kohut, E.J., Bloomer, S.H., Leybourne, M., Fouch, M., Vervoort, J., 2006. Subduction factory processes beneath the Guguan Cross-chain, Mariana Arc: no role for sediments, are serpentinites important? Contributions to Mineralogy and Petrology 151, 202–221.
Stromer Jr., J.C., 1983. The effects of recalculation on estimates of temperatures and oxygen fugacity from analyses of multicomponent iron-titanium oxides. American Mineralogist 68, 586–594.
Stosch, H.-G., 1982. Rare earth partitioning between minerals from anhydrous spinel peridotite xenoliths. Geochimica et Cosmochimica Acta 46, 793–811.
Sun, S.S., McDonough, W.F., 1989. Chemical and isotopic systematics of oceanic basalts: implications for mantle composition and processes. In: Saunders, A.D., Norry, M.J. (Eds.), Magmatism in the Ocean Basins: Geological Society. 42, pp. 313–345 London, Special Publication.
Takahashi, E., Uto, K., Schilling, J.G., 1987. Primary magma compositions and Mg/Fe ratios of their mantle residues along Mid-Atlantic Ridge 29 N to 73 N. Tech Rep Inst Study Earth's Interior Okayama University Ser A 9, 1–14.
Tan, W., Wang, C.Y., He, H.P., Liang, X.L., Liu, P., 2016. Mineralogy and origin of exsolution in the titanomagnetite of different magmatic Fe-Ti oxide bearing intrusions. Canadian Mineralogist 54, 539–553.
Thurston, P.C., 2015. Igneous rock associations 19. Greenstone belts and granite-Greenstone Terranes: constraints on the nature of the Archean world. Geoscience Canada 42, 437–484.
Toplis, M.J., Carroll, M.R., 1995. An experimental study of the influence of oxygen fugacity on Fe-Ti oxide stability, phase relations, and mineral-melt equilibria in ferro-basaltic systems. Journal of Petrology 36, 1137–1170.
Toplis, M.J., Corgne, A., 2002. An experimental study of element partitioning between magnetite, clinopyroxene and iron-bearing silicate liquids with particular emphasis on vanadium. Contributions to Mineralogy and Petrology144, 22–37.
Ulrych, J., 1986. Clinopyroxenes in the Cenozoic volcanic of the Ceske Stredohori MTS: A review. Acta Universitatis Carolinae 4, 367–376.
Ulrych, J., Cimbalnikova, A., Fiala, L., Kaspar, P., Lang, M., Minarik, L., Palivcova, M., Pivec, E., 1976. Petrology of the Petrovice melagabbro. Rozpr. Cs. Akad. Ved. R. Mat. Prir. Ved, Academia. Praha. 57 P.
Ulrych, J., Cimbalnikova, A., Fiala., L., Kaspar, P., Lang, M., Minarik, L., Palivcova, M., Pivec, E., 1976. Petrology of the Petrovice melagabbro. Rozpr. Ceskosl. Akad. Ved, Mat. Prirod. Tcheque Russe 86, 1–57.
Vincent, E.A., Phillips, I., 1954. Iron-titanium oxide minerals in layered gabbros of the Skaergaad intrusion. East Greenland. Geochimica et Cosmochimica Acta 6, 1–26.
Von Gruenwaldt, G., 1994. Ilmenite apatite enrichment in the upper zone of the Bushveld omplex: A major titanium rock phosphate resource. International Geology Review 35, 987–1000.
Wager, L.R., Brown, G.M., 1967. Layered igneous rocks. Oliver and Royd, Eginburgh 588 P.
Wehrmann, H., Hoernle, K., Jacques, G., Garbe-Schönberg, D., Schumann, K., Mahlke, J., Lara, L., 2014. Sulphur and chlorine geochemistry of mafic to intermediate tephras from the Chilean Southern Volcanic Zone (33–43°S) compared with those from the Central American Volcanic Arc. International Journal of Earth Sciences 103, 1945–1962.
Wells, P.R.A., 1977. Pyroxene thermometry in simple and complex systems. Ibid 62, 129–139.
Wood, B.J., Banno, S., 1973. Garnet-orthopyroxene and orthopyroxene–clinopyroxene relationships in simple and complex systems. Ibid 42, 109–124.
Xie, Q., Zhang, Z., Cheng, Z., Santosh, M., 2017. Interstitial microstructures in Ji'nan mafic intrusion, North China Craton: magmatic or hydrothermal origin? European Journal of Mineralogy 29, 839–850.
Yu, S., Yuwang, W., Jingbin, W., Hongjing, X., Qigui, M., Lutong, Z., Lingli, L., Dedong, L., Guochao, Z., 2018. Petrogenesis and Metallogenesis of the Niumaoquan Gabbroic Intrusion Associated with Fe-Ti Oxide Ores in the Eastern Tianshan, NW China. Acta Geologica Sinica 92 (5), 1862–1878.
Zhang, Z., Mao, J., Saunders, A.D., Ai, Y., Li, Y., Zhao, L., 2009. Petrogenetic modelling of three mafic-ultramafic layered intrusions in the Emeishan large igneous province, SW China, based on isotopic and bulk chemical constraints. Lithos 113, 369–392.
Zhou, M.F., Robinson, P.T., Lesher, C.M., Keays, R.R., Zhang, C.J., Malpas, J., 2005. Geochemistry, petrogenesis, and metallogenesis of the Panzhihua gabbroic layered intrusion and associated Fe-Ti-V oxide deposits, Sichuan Province, SW China. Journal of Petrology 46, 2253–2280.
Zimmer, M., 1989. Der Gebel Gerf-Komplex (Arabisch-Nubischer-Schild): petrographische und geochemische Untersuchungen eines spatproterozoischen Ophiolithes. Ph.D Dissertation, University of Mainz. Mainz, p. 192.
Zimmer, M., Kröner, A., Jochum, K.P., Reischmann, T., Todt, W., 1995. The Gabal Gerf complex: A Precambrian N-MORB ophiolite in the Nubian Shield, NE Africa. Chemical Geology 123, 29–51.
Zimmer, M.M., Plank, T., Hauri, E.H., Yogodzinski, G.M., Stelling, P., Larsen, J., Singer, B., Jicha, B., Mandeville, C., Nye, C.J., 2010. The role of water in generating the calc-alkaline trend: new volatile data for Aleutian magmas and a new tholeiitic index. Journal of Petrology 51, 2411–2444.